



1 **Precipitation of dolomite from seawater on a Carnian coastal plain (Dolomites, northern**
2 **Italy): evidence from carbonate petrography and Sr-isotopes**

3 Maximilian Rieder¹, Wencke Wegner², Monika Horschinegg², Stephanie Klackl¹, Nereo
4 Preto³, Anna Breda³, Susanne Gier¹, Urs Klötzli², Stefano M. Bernasconi⁴, Gernot Arp⁵,
5 Patrick Meister¹

6 ¹ Department of Geodynamics and Sedimentology, University of Vienna, Althanstr. 14, 1090 Vienna, Austria

7 ² Department of Lithospheric Research, University of Vienna, Althanstr. 14, 1090 Vienna, Austria

8 ³ Department of Geosciences, University of Padova, Via Gradenigo 6, 35131 Padova, Italy

9 ⁴ Geological Institute, ETH Zürich, Sonneggstr. 5, 8092 Zürich, Switzerland

10 ⁵ Geoscience Centre, University of Göttingen, Goldschmidtstr. 3, 37077 Göttingen, Germany

11 Correspondence: Patrick Meister (patrick.meister@univie.ac.at)

12

13 **Abstract.** The geochemical conditions conducive to dolomite formation in shallow evaporitic
14 environments along the Triassic Tethyan margin are still poorly understood. Most of the
15 Triassic dolomites in the Austroalpine and the South Alpine realm are affected by late
16 diagenetic or hydrothermal overprinting, but recent studies from the Carnian Travenanzes
17 Formation (South Alpine) provide evidence of primary dolomite. Here a petrographic and
18 geochemical study of the dolomites intercalated in a 100-m-thick Carnian sequence of distal
19 alluvial plain deposits is presented to gain better insight into the conditions and processes of
20 dolomite formation. The dolomites occur as 10- to 50-cm-thick homogenous beds, mm-scale
21 laminated beds and nodules associated with palaeosols. The dolomite is nearly stoichiometric
22 with slightly attenuated c-reflections. Sedimentary structures indicate that the initial primary
23 dolomite or precursor phase consisted largely of unlithified mud. Strontium isotope ratios
24 (⁸⁷Sr/⁸⁶Sr) of homogeneous and laminated dolomites reflect Triassic seawater, suggesting
25 precipitation in evaporating seawater in a coastal ephemeral lake or sabkha system. However,
26 the setting differed from modern sabkha or coastal ephemeral lake systems by seasonally wet
27 conditions with a significant siliciclastic input and inhibition of significant lateral groundwater



Sr-isotopes in Carnian primary dolomite

28 flow through impermeable clay deposits, thus representing a non-actualistic system in which
29 dolomite formed along the ancient Tethyan margin.

30

31 **Keywords** Dolomite, Sr-isotopes, sabkha, alluvial plain, peritidal platform, Travenanzes
32 Formation, ephemeral lake, authigenic carbonate.

33

34

35 **1 Introduction**

36 The formation of dolomite [CaMg(CO₃)₂] under Earth surface conditions in modern and
37 ancient environments is still a major unsolved problem in sedimentary geology. Dolomite
38 does not precipitate from modern open ocean water, apparently, because its nucleation and
39 growth is inhibited by a high kinetic barrier. For the same reason its precipitation under
40 laboratory conditions has been difficult (cf. Land, 1998), and therefore the factors that may
41 have influenced dolomite formation through Earth history, giving rise to a significant part of
42 the sedimentary record, also remain poorly constrained. Van Tuyl (1916) discussed several
43 competing theories, one of which was the chemical theory, where dolomite is a primary
44 precipitate, hence, forming as a result of the conditions prevailing in the depositional
45 environment. In contrast, stable isotope and fluid inclusion data often indicate that massive
46 dolomites formed due to replacement of precursor calcium carbonate during burial diagenesis,
47 i.e., at higher temperature and under conditions decoupled from the ancient depositional
48 environment. Chilingar (1965) suggested that the portion of dolomite in carbonates increases
49 with geological age, implying a replacement during burial. However, burial dolomitization
50 requires a mechanism pumping large volumes of Mg-rich water through porous rock (Machel,
51 2004) and is not always a viable process. There is evidence that at certain times in Earth's
52 history, large amounts of dolomite could have formed under near-surface conditions
53 (penecontemporaneous dolomite), and several studies linked the abundance of dolomite to



Sr-isotopes in Carnian primary dolomite

54 secular variations in seawater chemistry, with preferred dolomite formation during times of
55 "calcite seas" (Given and Wilkinson, 1987; Warren, 2000; Burns et al., 2000).

56 In the Tethyan realm, penecontemporaneous dolomite formation seems to have prevailed
57 during the Triassic (Meister et al., 2013, and references therein), in an "aragonite sea", while
58 elsewhere dolomite was not particularly abundant (cf. Given and Wilkinson, 1987). In Norian
59 shallow water dolomites of the Dolomia Principale, Iannace and Frisia (1994) measured
60 oxygen isotope values as positive as +3.5‰, suggesting a formation at Earth surface
61 temperatures, whereas dolomites of the overlying early Jurassic units typically show
62 signatures of burial diagenetic overprint. Frisia et al. (1994) interpreted these dolomites to be
63 an early diagenetic replacement of precursor carbonate. In a recent study, Preto et al. (2015)
64 suggested that the dolomites of the Carnian Travenanzes Formation (Fm.) in the Venetian
65 Alps are primary precipitates, i.e. they precipitated directly from a solution in the sedimentary
66 environment and not by replacement of a precursor phase during burial. This interpretation is
67 based on high-resolution transmission electron microscope (HR-TEM) analysis showing
68 nanometre-sized crystal aggregates within single micron-scale dolomite crystals. The nano-
69 crystal structures were not replaced by any of the dolomite phases described by Frisia and
70 Wenk (1993) in Late Triassic dolomites of the Southern Alps, and they show similarity to
71 dislocation-ridden Mg-rich phases observed in modern sabkha dolomite and interpreted as
72 primary (Frisia and Wenk, 1993). This finding is intriguing, not only because it is consistent
73 with primary dolomite formation already discussed by Van Tuyl (1916) and observed in many
74 modern environments (e.g., Sabkha of Abu Dhabi: Illing, 1965; Wenk et al., 1993; unlithified
75 dolomite is also mentioned in Bontognali et al., 2010; and Court et al., 2017; Deep Springs
76 Lake, California: Jones, 1965; Clayton et al., 1968; Meister et al., 2011; Coorong Lakes: Von
77 der Borch, 1976, Rosen et al., 1989, Warren et al., 1990; Brejo do Espinho, Brazil; Sánchez-
78 Román et al., 2009; Lake Acigöl, Turkey: Balci et al., 2016; Lake Neusiedl, Austria:
79 Neuhuber et al., 2015; Lake Van: McCormack et al., 2018), but it also provides a window into



Sr-isotopes in Carnian primary dolomite

80 ancient primary dolomite formation pathways. This finding is also consistent with recent
81 experiments by Rodriguez-Blanco et al. (2015), demonstrating a nano-crystalline pathway of
82 dolomite nucleation and growth. Critically, nanometre size nuclei show a different surface
83 energy landscape compared to macroscopic crystals, allowing for potentially lower energy
84 barriers, perhaps modified by organic matter, microbial effects, clay minerals or particular
85 water chemistry, and thus, promoting a spontaneous precipitation of dolomite.

86 The interpretation of primary dolomite in the Travenanzes Fm. needs further validation by
87 nano- and atomic scale analyses and further petrographic and geochemical investigations to
88 establish the environmental and geochemical conditions on this Carnian platform. In
89 particular, the origin of ionic solutions conducive to dolomite formation is still unclear.
90 Comparison with modern environments shows that ionic solutions may either be seawater-
91 derived, as shown for the sabkhas along the Persian Gulf coast, where several hydrological
92 mechanisms were discussed (Adams and Rhodes, 1960; Hsi and Siegenthaler, 1969;
93 McKenzie et al., 1980, McKenzie, 1981; see Machel, 2004, for an overview; cf. also Teal et
94 al., 2000), or derived from continental groundwater, as shown for the coastal ephemeral lakes
95 of the Coorong area (Australia; Alderman and Skinner, 1957; Von der Borch et al., 1976,
96 Rosen et al., 1989; Warren et al., 1990). While both types of fluid become concentrated
97 during evaporation and, perhaps, modified by the precipitation of carbonates and evaporites,
98 giving rise to abundant dolomite formation, it remains unclear which mechanism prevailed on
99 the Carnian platform.

100 The Travenanzes Fm. differs from these potential modern analogues in its large amounts of
101 clay. In fact, dolomites occur in the Travenanzes Fm. as beds intercalated in a 100-m-thick
102 sequence of red clay, deposited on a distal alluvial plain, presumably under seasonally wet
103 conditions. This facies shows, except for the horizons containing marine fossils, striking
104 similarity to a Germanic Keuper facies, which represents an extended and entirely continental
105 playa lake system, also showing intercalations of primary dolomite in red clay (Reinhardt and



Sr-isotopes in Carnian primary dolomite

106 Ricken, 2000). Although the Travenanzes Fm. is clearly located, palaeogeographically, in the
107 Tethyan depositional region (Breda and Preto, 2011), its facies separation from a Germanic
108 Keuper facies may not be precisely coincident with palaeogeographic features, such as the
109 Vindelician high zone. We suggest that the composition and origin of ionic solutions
110 conducive to primary dolomite formation, either from continental water or seawater, is also an
111 indicator for the palaeogeographic separation between the two facies zones.

112 Here we provide a detailed investigation of dolomites of the Travenanzes Fm. to
113 reconstruct the processes and factors conducive to dolomite formation. We specifically
114 searched for sedimentary structures indicating that the initially deposited authigenic carbonate
115 was still unlithified, as it would be expected if it spontaneously precipitated from the shallow
116 water bodies of ephemeral lakes or tidal ponds. Radiogenic Sr isotope ratios ($^{87}\text{Sr}/^{86}\text{Sr}$) were
117 measured in the dolomites and compared with the known Triassic seawater Sr-isotope curve
118 (Veizer et al., 1999; McArthur et al., 2012) to determine if the ionic solutions conducive to
119 dolomite formation are derived from seawater or from continental runoff. Values were also
120 compared to dolomites from modern environments and to dolomites of clear continental
121 origin from the Germanic Keuper. Based on the new insights we discuss possible scenarios of
122 dolomite formation that could have prevailed along the Triassic western Tethys margins and
123 in similar evaporative environments.

124

125 **2 Geological setting**

126 The Dolomite mountains (Southern Tyrol and Venetian Alps; Fig. 1a) are well known for
127 their characteristic peaks consisting of Triassic carbonate platform limestones and dolomites.
128 These platforms developed all along the margins of the western Tethys ocean (Stampfli and
129 Borel, 2002), and are separated by deep basins in the middle Triassic and form an extended
130 coastal plain during the Carnian and Norian. The Adriatic plate rotated by almost 90° counter
131 clockwise during alpine orogeny (Ratschbacher et al., 1991; Handy et al., 2010). As a result,



Sr-isotopes in Carnian primary dolomite

132 the deep-water environments are found to the north in today's tectonic position although they
133 were originally located to the east (Fig. 1a). In the Dolomites, the Triassic paleogeography
134 was largely preserved in spite of Alpine deformation because the Dolomites form a ca. 60 km
135 wide pop-up structure bound by the periadriatic line to the north and northwest and the
136 Valsugana fault to the southeast (Fig. 1a, inset). Therefore, the Dolomites were never buried
137 to greater depth and have not experienced a metamorphic overprint (Doglioni, 1987). The
138 colour alteration index of conodonts in the Heiligkreuz Fm., underlying the Travenanzes Fm.
139 in this region, is 1, suggesting maximum burial temperatures of less than 50°C which are
140 confirmed by biomarker data (Dal Corso et al., 2012).

141 The Travenanzes Fm. lies unconformably above the Heiligkreuz Fm., and is overlain by
142 the Dolomia Principale (Hauptdolomit) with a transgressive boundary (Fig. 1b). Presumably
143 as a result of a change in climate and increasing humid episodes during the Carnian, large
144 amounts of siliciclastic material were deposited, entirely filling the more than 100 m deep
145 basins between the carbonate platforms of the Cassian dolomite (Gattolin et al., 2013; 2015).
146 These basin-filling deposits form a coastal succession or mixed carbonate siliciclastic ramp,
147 including large clinofolds with sandstones and conglomerates (Heiligkreuz Fm.; see Preto
148 and Hinnov, 2003; Gattolin et al., 2013; 2015). The overlying Travenanzes Fm. was deposited
149 on an extremely flat topography, as it consists of ca. 100-m-thick red and green claystone with
150 intercalated dolomites, evaporites and siliciclastic beds (Fig. 2; Kraus, 1969; Breda and Preto,
151 2011). In a south-north transect, it shows a typical interfingering between alluvial deposits
152 with conglomerates and sandstones to the south and a carbonate-dominated peritidal to sabkha
153 facies to the north (Breda and Preto, 2011). The upper boundary to the Dolomia Principale is
154 time-transgressive, i.e., it becomes younger from north to south. The Travenanzes Fm.
155 consists of three transgressive-regressive cycles, with the highstand deposits showing
156 identical peritidal carbonate facies as the Dolomia Principale (Breda and Preto, 2011). The



Sr-isotopes in Carnian primary dolomite

157 boundary to the Dolomia Principale is defined by the last occurrence of siliciclastic material
158 (Gianolla et al., 1998).

159 The depositional environment of the siliciclastic facies in the Travenanzes Fm. has been
160 interpreted as a dryland-river system by Breda and Preto (2011). Such a system occurs in arid
161 environments if rivers drain into a coastal alluvial plain, but do not reach the coast.
162 Evaporation along the way may lead to the formation of playa lakes, whereas on the seaward
163 side extended evaporative tidal areas, i.e., sabkhas, develop. Both types of environment are
164 well known for giving rise to modern dolomite formation (see references above). As the
165 Southern Alps were located in tropical latitudes, a warm arid climate, perhaps influenced by a
166 monsoon effect, had developed (Muttoni et al., 2003). Rivers provided large amounts of clay,
167 becoming partially oxidized under subaerial conditions, a typical red and green clay
168 succession containing palaeosols developed.

169 This facies is widespread throughout the Alpine and Tethyan realm during the Carnian, but
170 the same deposits are strongly deformed by alpine tectonics in most Austroalpine units,
171 forming a characteristic band of rauhacke, the “Raibl beds” (e.g., Czurda and Nicklas,
172 1970). In the Travenanzes Fm. the entire sequence still shows its depositional architecture,
173 providing a pristine archive to study the diverse intercalated dolomites.

174 The Carnian and Norian deposits of the Keuper in the endorheic Germanic Basin show a
175 similar facies as the Travenanzes Formation. The Germanic deposits are described in more
176 detail by Reinhardt and Ricken (2000; and references therein), and they clearly represent
177 continental playa lake deposits. Here they are only included for comparison with the
178 Travenanzes Formation.

179

180 **3 Methods**

181 **3.1 Petrographic and mineralogical analysis**



Sr-isotopes in Carnian primary dolomite

182 A total of 39 hand specimens were collected from the stratigraphic section at Rifugio
183 Dibona 5 km west of Cortina d'Ampezzo (46.532727N/12.067161E; Fig. 1; Breda and Preto,
184 2011). Additional samples of Triassic dolomites from the Germanic Basin (Weser Fm. and
185 Arnstadt Fm. near Göttingen, Northern Germany) and modern dolomite from the Coorong
186 Lagoon (South Australia) and Deep Springs Lake (California) were also analysed for
187 comparison. Polished thin sections were carbon coated for analysis under the scanning
188 electron microscope (SEM) using a FEI Inspect S-50 SEM (Thermo Fisher Scientific,
189 Bremen, Germany). Element contents were determined semi-quantitatively using an EDX
190 detector (EDAX Ametek, New Jersey, United States) under high vacuum, a spot size 5.0 and
191 12.5 kV beam voltage at a working distance of 10 mm. Differences in mineralogy at the
192 micron scale were mapped in backscatter mode with high contrast.

193 For bulk mineralogical analysis three dolomite samples were milled with a disk mill. Clay
194 mineralogy was determined on 40 g aliquots that were leached two times for 24 h in 250 ml of
195 25% acetic acid to dissolve all carbonate (Hill and Evans, 1965). The clay mineral separates
196 were washed three times with H₂O and centrifuged. The grain size fraction <2 µm was
197 collected by sedimentation in an Atterberg cylinder after 24 h 33 min. Oriented samples were
198 prepared by pipetting the suspensions (10 mg clay/ml) on glass slides and analysed after air
199 drying. To identify expandable clay minerals, the samples were additionally saturated with
200 ethylene-glycol and heated to 550°C (Moore and Reynolds, 1997). X-ray diffraction analysis
201 of bulk samples and clay mineral separates was performed with a PANalytical X'Pert Pro
202 diffractometer using CuK α radiation with 40 kV and 40 mA. The samples were scanned from
203 1.76° to 70° 2 θ with a step size of 0.0167° and 5 s per step. The X-ray diffraction patterns
204 were interpreted using the Panalytical software "X'Pert High score plus" and Moore and
205 Reynolds (1997) for the clay minerals.

206 Total organic carbon (TOC) and total inorganic carbon (TIC) contents were determined for
207 seven samples of pure claystone, not containing any dolomite layers or nodules. This material



Sr-isotopes in Carnian primary dolomite

208 was used as carbonate-free control for acid leaching experiments as explained below. Ca. 0.2
209 g of dry sample powder was measured in a LECO RC-612 multiphase carbon analyser, at the
210 Department of Environmental Geosciences at the University of Vienna, with a temperature
211 ramp of 70°C per min to a maximum temperature of 1000°C.

212

213 **3.2 Carbon and oxygen isotope analysis**

214 Carbon and oxygen isotopes were measured on 28 samples which were micro-drilled
215 from thin section cuttings (see below). The samples were analysed with a Delta V Plus mass
216 spectrometer coupled to a GasBench II (Thermo Fisher Scientific, Bremen, Germany) at the
217 ETH Zürich (Zürich, Switzerland) following the procedure described in Breitenbach and
218 Bernasconi (2011). The precision was better than 0.1‰ for both isotopes. The oxygen isotope
219 values were corrected for kinetic fractionation during dissolution of dolomite in anhydrous
220 phosphoric acid at 70°C, using a fractionation factor of 1.009926 (Rosenbaum and Sheppard,
221 1986).

222

223 **3.3 Element analysis**

224 Total element concentrations were measured in leachates of the same three dolomite
225 specimen analysed by XRD and two claystones with the lowest inorganic carbon content. The
226 purpose of these measurements was to test the efficiency of the sequential extraction
227 procedure used for Sr-isotope analysis, and to determine potential origins of the Sr. The
228 samples were homogenized in an agate pestle and mortar and 100 mg of the homogenized
229 powder were weighed into centrifuge tubes. The samples were reacted in 10 ml 0.1 N acetic
230 acid and placed on a shaker for two days. The sample was centrifuged and the supernatant
231 was stored separately. The leaching step was repeated with 10 ml of 1 N acetic acid. Five ml
232 of each fraction were used for element concentration analysis (the rest was further processed
233 for Sr-isotope analysis; see below). The solutions were evaporated on a heating plate and the



Sr-isotopes in Carnian primary dolomite

234 residues were redissolved in 5 ml 2.5 N HNO₃. This step was repeated with 5 ml 5% HNO₃.
235 Concentrations were measured with a Perkin Elmer 5300 DV ICP-OES at the Department for
236 Environmental Geosciences (University of Vienna). Detection limits for the different
237 elements in rock (µmol/g) were: Al: 0.185, Ca: 0.025, Fe: 0.090, K: 0.026, Mg: 0.041, Mn:
238 0.002, Na: 0.004, P: 0.032, Ti: 0.002, Ba: 0.001, Sr: 0.001 and Rb: 0.012. The precision of the
239 measurements (relative standard deviation; RSD) for the elements Al, Ca, K, Mg, Ti, Ba and
240 Sr was ≤0.9% and for the elements Fe, Mn, Na, Rb, P it was ≤6.8%.

241

242 **3.4 Radiogenic Sr-isotope analysis**

243 To ensure that Sr from the pure dolomite phase is extracted specific areas free of clay
244 minerals were recognized by SEM and identified using an Olympus SZ61 microscope
245 equipped with a MicroMill sampling system (Electro Scientific Industries). Eleven samples
246 were drilled over a square area of 5-10 mm², or along a line in laminated rocks, to a depth of
247 350 µm. To prevent the powder from being blown away, the samples were drilled within a
248 drop of MilliQ-H₂O, and the suspension was transferred to a centrifuge tube using a pipette.
249 Also bulk samples, clay samples, pure celestine and barite purchased from W. Niemetz
250 (Servitengasse 12, 1090 Vienna, Austria), pure dolomite powder from Alfa Aesar (Thermo
251 Fisher – Kandel – GmbH, Postfach 11 07 65, 76057 Karlsruhe, Germany) and a fragment of a
252 single dolomite crystal were analysed as controls. They were crushed to a powder in an agate
253 mortar and pestle. Dolomite, barite, and celestine were mixed in a similar ratio as they occur
254 in the dolomites of the Travenanzes Fm. and run through the entire procedure as a control of
255 extraction efficiency. 14 mg of rock powder was weighed out for isotope analysis.

256 As additional precaution to extract the most pure dolomite phase for Sr-isotope analysis, a
257 sequential extraction was used. The extractions were routinely performed in 2 ml or 15 ml
258 polypropylene tubes with cap at room temperature on a shaker for 10 min to 24 h. The
259 following leaching reagents (always 2 ml) were used: 1 M NaCl, 3.3 M KCl, 0.1 N acetic



Sr-isotopes in Carnian primary dolomite

260 acid, 1 N acetic acid and 6 N HCl. Each reaction step was repeated once, and the residues
261 were washed with 2 ml of MilliQ H₂O after each step to remove remains of the previous
262 solvent.

263 Sr was separated from interfering ions (e.g. Fe, K, Rb and Ca) using an ion exchange
264 column packed with BIO RAD AG 50W-X8 resin (200-400 mesh, hydrogen form). Leachates
265 were evaporated, dissolved in 6 N HCl and 2.5 N HCl and loaded to the column in 2 ml 2.5 N
266 HCl. Then 51 ml of 2.5 N HCl were run through the column to wash out the interfering ions.
267 The Sr was eluted with a further 7 ml 2.5 N HCl and dried after collection. Total procedural
268 blanks for Sr were <1 ng and were taken as negligible (the amounts of strontium in the
269 samples were always higher than 100 ng).

270 The isotopic composition of Sr was measured with a Triton (Thermo Finnigan) thermal
271 ionisation mass spectrometer. Sr fractions were loaded (dissolved in 1 µl H₂O) as chlorides
272 and vaporized from a Re double filament. The double filament configuration was used to
273 accelerate detachment of the Sr from the filament. The cup configuration was calibrated such
274 that masses 84, 85 (centre cup), 86, 87 and 88 are detected. The NBS987 Sr isotope standard
275 (number of replicates = 40) shows a ⁸⁷Sr/⁸⁶Sr-ratio of 0.710272 ±0.000004 during the time of
276 investigation, with the uncertainty of the Sr isotope ratios quoted as 2σ. Interference with ⁸⁷Rb
277 was corrected using a ⁸⁷Rb/⁸⁵Rb ratio of 0.386. Within-run mass fractionation was corrected
278 for ⁸⁶Sr/⁸⁸Sr = 0.1194.

279

280 4 Results

281 4.1 Petrographic description of dolomites

282 Fig. 2 shows the distribution of the different types of dolomite through the 100-m-thick
283 lower, clay-rich interval of the Travenanzes Fm., above which the facies switches sharply to
284 massive bedded dolomites similar to those of the overlying Dolomia Principale.
285 Macroscopically three types of dolomite can be distinguished: homogenously bedded



Sr-isotopes in Carnian primary dolomite

286 dolomite, laminated dolomite, and nodular dolomite (Fig. 3a-c). The lower and middle part of
287 the clay-rich series harbours mainly homogeneous dolomite beds in red clay. Between 40 and
288 70 m several horizons with gypsum nodules occur (Fig. 3d). A 30-cm-thick fluvial
289 conglomerate with dolomite-cemented quartzarenites and pebbles of ripped up micritic
290 carbonate occurs at 75 m (Fig. 3e), above which palaeosols with dm-scale vertical pedes,
291 possible root traces showing green reduction haloes, and nodular dolomite (calcic vertisols;
292 cf. Cleveland et al., 2008), are more frequent (e.g., Fig. 3b). Tempestite beds with
293 megalodonts, foraminifers and ostracods occur at 65 and 89 m. A pronounced transition
294 occurs in the uppermost ca. 8 metres of the clay-rich interval (Fig. 2b), where the clay entirely
295 changes from red to grey colour (Fig. 2c), and laminated dolomites become predominant
296 while evaporites and palaeosols are absent. The laminated dolomites (Fig. 3c) and cm- to dm-
297 scale dolomite-clay interlayers show intense slumping and soft sediment deformation and
298 pseudo-teepee structures (Figs. 3f, g). Here we provide a short summary of the petrographic
299 analysis of thin sections of the different types of dolomite with the most important features
300 compiled in table 1.

301

302 *Homogenous dolomites*

303 Homogeneous dolomite beds are usually 10 cm to 50 cm thick, embedded within clays and
304 with sharp, plane-parallel joints. They consist of dolomicrite, which was described as
305 aphanotopic dolomite by Breda and Preto (2011), according to the extended nomenclature for
306 dolomite fabrics by Randazzo and Zachos (1983). The sediment is matrix-supported and
307 contains irregular, partially rounded mud clasts (intraclasts) that consist of an aphanotopic
308 dolomite as the matrix. Some of the mud clasts contain smaller and somewhat darker
309 mudclasts or peloids (Fig. 4a, arrow). Soft sediment deformation is often not clearly visible
310 due to the homogeneous structure of the mud, but it can be observed where the mud clasts are
311 deformed within the matrix (Fig. 4b). Some of the homogeneous beds in the lower part of the



Sr-isotopes in Carnian primary dolomite

312 section show sub-millimetre lamination that is only visible under the microscope, where it
313 appears as an alternation of light (locally coarser) and dark aphanotopic dolomite.

314 The clay content in the homogeneous beds is generally low. A few beds (e.g. at 33.5 m in
315 the section) consist of silty or sandy dolomite, as reflected in a high abundance of detrital
316 quartz in thin section. Pseudomorphs after gypsum occur in a dolomite bed at 120 m (Fig. 4c,
317 d). Moldic porosity occurs in three layers at 43, 65 and 89 m, within aphanotopic dolomite.
318 These are the tempestite beds observed in the outcrop (cf. Breda and Preto, 2011).

319 One homogenous dolomite bed located at 64 m in the section contains oolitic grainstone,
320 lacking both an aphanotopic and a cement matrix (Fig. 4e). Ooids are either hollow (where
321 the cores may have been dissolved) or filled with sparite and are surrounded with an
322 isopachous cement rim.

323

324 *Nodular dolomites*

325 Nodular dolomites (Fig. 3b) often occur in beds of vertical peds linked to palaeosols as
326 indicated by horizons of typical vertical cracks showing green alteration fronts. Single
327 nodules also may sporadically occur embedded within metre-thick beds of red and green clay.
328 Nodules are usually 5 to 10 cm in size, consist of aphanitic dolomite or occasionally
329 somewhat coarser microspar, and in cross section show both red and pale areas. Most
330 nodules also show a deformed or brecciated internal structure with the interstices between the
331 clasts mostly consisting of matrix and clay cutans.

332

333 *Laminated dolomites*

334 Laminated dolomites occur in the upper part of the clay rich interval, between 90 and 110
335 m in the section (Fig. 4f-i). In the field, they show an alternation of light grey dolomite
336 laminae and dark grey to black clay laminae in the mm-range. Some dolomite laminae show
337 upward bending reminiscent of pseudo-teepee structures (Fig. 4f), and the space within the



Sr-isotopes in Carnian primary dolomite

338 teepee is sometimes infilled with sparry cement. Also, the bending of the laminae towards the
339 upward directed cusps is reminiscent of load structures (dish structures), but they also may
340 represent desiccation cracks. The laminae are frequently ripped apart and fragments of
341 laminae occur reworked as flat pebbles embedded in an aphanotopic dolomite matrix (Fig.
342 4g). Some laminae show a microsparitic appearance and laminar fenestral porosity. In some
343 laminae a peloidal fabric is observed (e.g in Fig. 4f). Laminae are typically graded, whereby
344 the upper part is darker, indicating an increase in the clay content (Fig. 4h, i). The top of the
345 laminae is often truncated by an erosion surface, and rip-up clasts of the fine mud (mud
346 clasts) are embedded in the overlying coarse layer. Some laminated dolomites contain
347 continuous layers with inclusions of celestine crystals in the 100- μm -range, some of them
348 with barite in their centre (Fig. 5a-c). Occasionally also pyrite occurs.

349 Under the SEM, laminated dolomites show an anhedral structure in the 1-5 μm range. No
350 difference in mineral structure and grain size is usually observed between mud clasts and the
351 surrounding, often lighter-coloured matrix. Dolomite crystals at the margins between
352 dolomite and clay interlayers often coalesce into 5- μm -scale round aggregates consisting of
353 several subhedral crystals with different orientation (Fig. 6a, b; the crystals show orientation
354 contrast under BSE mode). Dolomite crystals are often porous, showing a somewhat
355 disordered appearance, but they are surrounded by syntaxial rims. In most cases, the rims
356 entirely fill the intercrystalline space, forming almost hexagonal compromise boundaries (Fig.
357 6c, d). These rims occur both in homogeneous and laminated dolomites.

358

359 *Germanic Keuper dolomites*

360 A sample from the Carnian Lehrberg Beds (middle Lehrberg bed; clay pit Friedland, 12
361 km south of Göttingen, Northern Germany; Seegis, 1997; Arp et al., 2004) shows a brittle
362 structure with high porosity. The material consists mainly of packed ooids or rarely peloids in



Sr-isotopes in Carnian primary dolomite

363 a sparitic cement matrix. Under the SEM, subhedral to euhedral dolomite in the 5- μ m-range
364 are observed within the ooids (not shown).

365 A sample from the Norian Arnstadt Fm. (formerly termed “Steinmergelkeuper”; middle
366 grey series; locality of Krähenberg, 11 km SSW of Göttingen, Northern Germany; Arp et al.
367 2005) shows a mm-scale lamination and cm- to dm-sized laminated clasts, which were
368 interpreted as a stromatolite breccia. The laminae contain abundant agglutinated siliciclastic
369 grains (mainly quartz, subordinate albite) and phosphoritic fish scales. The dolomicrite shows
370 a subhedral structure in the ≤ 5 μ m range with a few larger subhedral grains resulting in a
371 porphyrotopic fabric (not shown).

372

373 4.2 Mineralogy

374 Bulk dolomite shows a position of the 104 peak at a mean d-value of 2.88816 Å (Fig. 7a;
375 Table 2). This indicates a Ca content of 50.7%, based on the equation of Lumsden (1979).
376 The structural order is indicated by the ratio of the superlattice-ordering peak at (015) to the
377 (110) ordering peak. The height ratio is 0.44, which is near to 0.519 (Table 2) indicated for an
378 ordered dolomite in the Highscore database.

379 Clay mineral analysis (Fig. 7b-d) revealed illite in samples TZ14-1 and TZ14-7 and an R3
380 ordered illite-smectite mixed-layer clay mineral in sample TZ14-9. In the ethylene-glycol-
381 saturated state, the broad shoulder at 11.4 Å contains components of the illite 001 reflection
382 and of the fourth order of a 47 Å superstructure peak whose unit cell consists of three 10 Å
383 illite layers and one 17 Å smectite layer (Moore and Reynolds, 1997). This smectite
384 component was not observed in samples TZ14-1 and TZ14-7.

385

386 4.3 Carbon content

387 Total carbon contents in shales (Table 3) range from 0.06 to 0.51 wt%. Samples TZ16-1
388 und TZ16-19B showing the lowest TIC of 0.02 wt% were selected as controls to test for



Sr-isotopes in Carnian primary dolomite

389 $^{87}\text{Sr}/^{86}\text{Sr}$ -ratios of Sr potentially adsorbed to clay minerals. TOC-contents are in the range of
390 0.05 - 0.16 wt%. Max. TIC-values are 0.46 wt%.

391

392 **4.4 Carbon and oxygen isotopes**

393 Carbon isotope values vary between -3.38 and +4‰ VPDB. Oxygen isotope values are
394 between -0.7 and +0.9‰ VPDB (three outliers show values as low as -1.5‰ VPDB; Table 4;
395 Fig. 8a). A clear distinction occurs between nodular dolomites showing negative $\delta^{13}\text{C}$ -values
396 and homogeneous dolomites showing positive values. Laminated dolomites show
397 intermediate values and low variability. The oxygen isotopes show an upward increasing
398 trend (Fig. 8b). The calculated temperature of formation assuming a Triassic seawater
399 composition of -1‰ VSMOW using the fractionation equation of Vasconcelos et al. (2005)
400 shows temperatures between 29 and 39°C. A more positive value of the water would result in
401 higher temperatures.

402

403 **4.5 Element composition of the dolomites**

404 Concentrations of the elements Al, Ca, Fe, K, Mg, Mn, Na, P, Ti, Ba, Sr, and Rb (mmol/g
405 sample) are shown in Table 5. Ca contents are between 1.68 and 2.33 mmol/g in the 0.1 N
406 acetic acid fraction and between 2.71 and 2.87 mmol/g in the 1 N acetic acid fraction. Mg
407 contents are between 1.61 and 2.34 mmol/g in the 0.1 N acetic acid fraction and between 2.48
408 and 2.64 mmol/g in the 1 N acetic acid fraction. Based on these concentrations, the amount of
409 dolomite dissolved is between 30 and 43 wt% of the bulk sample in the 0.1 N acetic acid
410 fraction and between 49 and 52 wt% in the 1 N acetic acid fraction of the sequential
411 extraction. In total, between 84 and 90 wt% of the bulk sample were dissolved during these
412 two extraction steps. If molar concentrations of Ca are plotted vs. Mg a linear trend with a
413 slope of 0.935 is observed (Fig. 9a), indicating 48.3 mol% MgCO_3 in the dolomite phase.



Sr-isotopes in Carnian primary dolomite

414 The Sr-concentrations in bulk dolomite samples are in the range of 0.38 and 1.16 $\mu\text{mol/g}$
415 in the 0.1 N acetic acid fraction and between 0.57 and 0.79 $\mu\text{mol/g}$ in the 1 N acetic acid
416 fraction (except one extremely high value of 34.91 $\mu\text{mol/g}$ in sample TZ14-9). These contents
417 are much higher than in pure clay mineral samples with 0.047-0.417 $\mu\text{mol/g}$ in the 0.1 N
418 acetic acid fraction and even lower concentrations (<0.19 $\mu\text{mol/g}$) in the other fractions. In
419 all samples measured by ICP-OES, rubidium (Rb) concentrations are below the detection
420 limit of 0.012 $\mu\text{mol/g}$.

421 Correlation of Sr contents to other elements did not show clear trends. In particular, Sr-
422 content did not correlate with Mg or Ca. Sr correlates with K (Fig. 9b), but at the same time,
423 K is extremely low in all clay mineral leachates.

424

425 **4.6 Sr-isotopes**426 *$^{87}\text{Sr}/^{86}\text{Sr}$ -ratios of pure minerals*

427 Results of Sr-isotope measurements are listed in Table 6. Repeated extractions of
428 chemically pure dolomite reference material dissolved in 0.1 N acetic acid showed a range of
429 $^{87}\text{Sr}/^{86}\text{Sr}$ -ratios between 0.709942 ± 0.000011 and 0.710831 ± 0.000007 . Pure single crystals of
430 dolomite extracted sequentially showed the highest value (0.708401 ± 0.000040) in the 1 M
431 NaCl fraction. Values in the 0.1 N acetic acid fraction (0.707735 ± 0.000006) and the 1 N
432 acetic acid fraction (0.707666 ± 0.000006) are lower by almost 0.001 than in the NaCl
433 fraction.

434 In pure barite, $^{87}\text{Sr}/^{86}\text{Sr}$ -ratios decrease by about 0.0013 in the extraction sequence from 0.1
435 N acetic acid to 6 N HCl. Celestine is highly soluble and was only measured in the 1 M NaCl
436 fraction and one time in 0.1 N acetic acid. It shows similar values as in the 1 M NaCl fraction
437 of the pure barite-celestine-dolomite mixture (0.708038 ± 0.000003), but the latter increased to
438 0.709501 ± 0.000040 in the 0.1 N acetic acid fraction.



Sr-isotopes in Carnian primary dolomite

439

440 *⁸⁷Sr/⁸⁶Sr-evolution during sequential extraction of dolomites of the Travenanzes Fm.*

441 Different modifications of the sequential extraction were investigated using three samples
442 (TZ14-1, TZ14-7 and TZ14-9; Table 6). ⁸⁷Sr/⁸⁶Sr-ratios decrease in sample TZ14-1 from
443 0.708125 ±0.000012 to 0.707666 ±0.000004 with increasing strength of the leaching reagent,
444 while the values remain almost constant in sample TZ14-9. However, repeating the 0.1 N
445 acetic acid extraction (for 36 h) after a rather intense first extraction (4h, 12h, 4h) resulted in
446 extremely high values (0.715417 ±0.000250 in TZ14-1 and 0.7192266 ±0.000455 in TZ14-9).
447 Standard deviations are also higher than in the other fractions.

448 The sequential extractions were repeated, whereby the Sr-concentrations were determined
449 by ICP-OES (see section above). In addition, 1 N acetic acid and 6 N HCl fractions were
450 extracted. Results are similar to the previous extraction sequences, but the values further
451 decreased in the 1 N acetic acid fraction. Only the HCl-fraction showed very high values of
452 0.730453 ±0.000005 in sample TZ14-7.

453 Sequential extractions of the clay samples from the Travenanzes Fm. show a similar
454 increase with the sequential extraction steps from 0.1 N acetic acid fraction to 6 N HCl, where
455 ⁸⁷Sr/⁸⁶Sr-ratios reach similar values as in the dolomite extracts (from 0.722998 ±0.000018 to
456 0.733910 ±0.000024).

457

458 *⁸⁷Sr/⁸⁶Sr-ratios in micro-drilled dolomite*

459 Eleven dolomite samples were micro-drilled from areas where dolomite was most pure
460 based on examination by SEM and dissolved in 0.1 N acetic acid. The values of the
461 Travenanzes Fm. are in the range of 0.707672 ±0.000003 to 0.707976 ±0.000004. The highest
462 value occurs in a dolomite nodule, while no systematic difference between homogenous and
463 laminated dolomite was observed. Dolomite of the Germanic Keuper samples shows much
464 higher ⁸⁷Sr/⁸⁶Sr-ratios of 0.709303 ±0.000006 and 0.709805 ±0.000005, respectively.



Sr-isotopes in Carnian primary dolomite

465

466 *⁸⁷Sr/⁸⁶Sr-ratios of modern dolomites (Deep Springs Lake, Coorong Lakes)*

467 Dolomites of Deep Springs Lake show strongly radiogenic values of 0.713086 ± 0.000004
468 and 0.713207 ± 0.000004 , which are much higher than modern seawater values, showing a
469 ⁸⁷Sr/⁸⁶Sr-ratio of 0.709234 ± 0.000009 (DePaolo and Ingram, 1985). In contrast, dolomite from
470 the Coorong Lakes (Milne Lake) shows ratios between 0.709251 ± 0.000004 and 0.709275
471 ± 0.000003 , which is very near to modern seawater. Different incubation times (5 min und 10
472 h) in 0.1 N acetic acid had no influence on the isotope ratios.

473

474 **5 Discussion**475 **5.1 Interpretation of microfacies within different types of dolomite**476 *Homogeneous dolomite beds*

477 The homogeneous dolomite beds, which are mainly intercalated in the lower, clay-rich part
478 of the Travenanzes Fm., consist of fine-grained dolomicrite (aphanotopic dolomite), with
479 occasional intraclasts of the same aphanotopic dolomite as the matrix. Soft sediment
480 deformation and dolomicrite infill between mud clasts indicate that this sediment consisted to
481 a large extent of unlithified carbonate mud. Based on the abundance of fine mud, water
482 energy was probably not very high (Demico and Hardie, 1994), although reworking and
483 partial rounding of the mud clasts require at least occasionally higher water energies.
484 According to the standard microfacies concept this type falls into SMF 23 (“non-laminated
485 homogeneous micrite and microsparite without fossils”), indicating a deposition in “saline
486 and evaporative environments, e.g. in tidal ponds” (Flügel, 2010). Also, SMF 24 (“lithoclastic
487 floatstones, rudstones and breccias”) is observed in some of the beds where mud clasts are
488 abundant. These facies types are consistent with supersaturation-driven precipitation of a fine-
489 grained authigenic carbonate in environments partially restricted from open seawater and
490 would match both with a coastal sabkha environment and/or with shallow ephemeral lakes.



Sr-isotopes in Carnian primary dolomite

491 Ephemeral lakes may have formed on extended coastal alluvial plains along the Tethyan
492 margin during the Carnian. The fine mud may have been homogenized and redistributed due
493 to minor wave action in the ponds (cf. Ginsburg, 1971).

494 In a semi-arid climate, episodic flooding of the alluvial plains by river water, which
495 however mostly evaporated before reaching the coast, led to the formation of a dryland river
496 system (Breda and Preto, 2011). The fluvial system may have supplied water to temporally
497 existing evaporating ponds. Alternatively, the alluvial plain may have been sporadically
498 flooded by seawater, explaining the intercalations of authigenic dolomite layers in the
499 succession of alluvial clays. Homogeneous dolomites show a positive carbon isotope
500 signature between 0.7 and 4‰ VPDB (except one outlier), which would be consistent with
501 formation from unaltered marine carbon in evaporative brine, with no significant contribution
502 of ^{12}C derived from organic matter. As indication of evaporative conditions, several gypsum
503 beds occur between 45 and 70 m in the section, and pseudomorphs after gypsum were
504 observed in a thin section of a dolomite at 120 m (Fig. 4c, d). But evaporites may not always
505 be preserved as they were most likely dissolved due to seasonally wet conditions.

506 While most homogeneous dolomite beds consist of aphanitic dolomite, a bed of dolomitic
507 ooid grainstone devoid of matrix occurs at 64 m (Fig. 4e), and tempestites showing moldic
508 porosity indicative of dissolved allochems and dissolved fossils occur at several levels in the
509 section. These beds must represent events of higher water energy, contributing sediment from
510 more open marine areas. The presence of marine fossils, such as *Megalodon*, indicate that at
511 least episodically the environment was marine influenced. The microfacies of the oolite falls
512 into SMF 15, which indicates proximity to the seaward edge of the platform. A similar facies,
513 however, is encountered in the Carnian Lehrberg Beds (Seegis, 1997) in a lacustrine setting.
514 Several beds containing abundant siliciclastic material (mainly angular quartz clasts) are more
515 likely due to a riverine flooding event, providing detrital material from the continent. Thus,



Sr-isotopes in Carnian primary dolomite

516 the microfacies in homogenous dolomite beds indicates both marine and continental influence
517 on the depositional environment.

518

519 *Laminated dolomite*

520 In the upper part of the clay-rich interval, predominantly laminated dolomites reminiscent
521 of loferites (Fischer, 1964) occur. The change from more homogeneous to laminated dolomite
522 intercalations correlates with the change from red to dark grey clay. The lamination consists
523 of millimetre-scale dolomite/clay interlayers suggesting an alternation of clay and fine
524 dolomite deposition. The microfacies falls into SMF 25 (“laminated evaporite-carbonate
525 mudstone facies”) indicating an “upper intertidal to supratidal sabkha facies in arid and
526 semiarid coastal plains and evaporitic lacustrine basins” (Flügel, 2010). Laminae showing soft
527 sediment deformation could not be attributed to stromatolitic bindstone facies (SMF 19 to 21).
528 Only some layers showing a coarser fabric with interstitial dolosparite or dolomicrosparite
529 containing putative peloids have been interpreted as microbial laminites (Preto et al., 2015).
530 Mostly, graded bedding indicates a direct sedimentation process rather than in situ
531 precipitation of the primary carbonate within a microbial mat (Vasconcelos et al., 2006;
532 Bouton et al., 2016; Court et al., 2017; Perri et al., 2018). A detrital origin of the clay in the
533 dolomites is confirmed by the well-ordered illite-smectite mixed-layer composition which
534 would be atypical for authigenic clay minerals. Frequent subaerial exposure and desiccation
535 may explain why the sediment was not homogenized and the lamination is preserved. This is
536 supported by the occurrence of pseudo-teepee structures as remnants of desiccation cracks.
537 Rip-up clasts were formed during subsequent flooding, whereby angular flat pebbles occur
538 where the sediment was desiccated or partially lithified. However, laminae also show
539 frequently plastic deformation (e.g. in Fig. 3g) where the mud was still unlithified.

540 Some uncertainty exists as to whether the facies was peritidal or represents ephemeral
541 lakes, as suggested for the homogeneous dolomites above. Episodic high water-energy



Sr-isotopes in Carnian primary dolomite

542 indicated by the rip-up clasts, combined with frequent desiccation, could point to evaporative
543 tidal conditions, as they occur in a sabkha. What is atypical for a modern sabkha is the large
544 amount of detrital input. But this is owed to the seasonally wet conditions during the Carnian
545 and the facies can be considered a mixed facies of alluvial plain and coastal sabkha: a “dirty”
546 sabkha. Under such conditions, the large amounts of evaporites, in particular gypsum, as they
547 usually occur in a sabkha, could have been dissolved. Why the occurrence of laminated
548 dolomites coincides with the transition from red to grey clays is not clear but may be related
549 to more permanently water-saturated conditions in the subsurface, while the surface was
550 exposed to periodic desiccation. Also this would be consistent with a sabkha environment.

551

552 *Nodular dolomite*

553 The clay beds were subject to strong evaporation and vadose diagenesis causing oxidation
554 and red colour. This generally indicates, at least seasonally, arid conditions. Dolomite nodules
555 that occur sporadically within certain intervals show internal brecciation, which probably
556 occurred after sedimentation. Internal brecciation is a typical feature of present day calcretes
557 in arid environment (e.g. Mather et al., 2018). Slightly negative $\delta^{13}\text{C}$ -values indicate a
558 contribution of carbon derived from organic matter degradation, suggesting that they formed
559 within the sediment. Presumably the formation of dolomite nodules could be related to
560 diagenesis in palaeosols. In the upper part of the section (between 80 and 105 m) dolomite
561 nodules are associated with green reaction haloes along vertical peds in palaeosols of vertisol-
562 calcisol type (Preto et al., 2015). Carbonate formation may have been related to reducing
563 fluids in water-logged soils during humid intervals, while the crack formed during desiccation
564 in dry periods, perhaps facilitated by the presence of expandable clay minerals (smectite).

565

566 **5.2 The origin of ionic solutions conducive to dolomite formation**

567 Overall, the dolomites in the Travenanzes Fm. show facies that match a variety of potential



Sr-isotopes in Carnian primary dolomite

568 depositional environments. They show some similarity to the Germanic Keuper, and it is not
569 entirely clear from the facies, whether a marine influence occurred, except if indicated by
570 marine fossils, as in the tempestite beds. To better trace the origins of ionic solutions to the
571 environments that were conducive to dolomite formation, Sr-isotopes were analysed.

572

573 *Strontium derived from seawater*

574 Radiogenic $^{87}\text{Sr}/^{86}\text{Sr}$ ratios can be indicative of the source of ionic solutions from which the
575 dolomite precipitated (Müller et al., 1990a; Müller et al., 1990b). Sr-isotopes in selected
576 dolomites through the Travenanzes Fm. at the Dibona section showed values between
577 0.707672 ± 0.000003 and 0.707976 ± 0.000004 . We correlate the Dibona section (Fig. 10) with
578 the Carnian seawater curve (Korte et al., 2003). Although the age interval of the Travenanzes
579 Fm. is not precisely constrained, findings of ammonites at the base of the succession suggest a
580 Tuvalian II age (*subbullatus* zone, 232.5-231.0 Ma; Ogg, 2012). The upper boundary of the
581 Travenanzes Fm. is time-transgressive and hence the age not precisely constrained. We
582 assume that the sedimentation rate was at least as high, or higher, than in the peritidal
583 carbonates of the Dolomia Principale. In this region, the Dolomia Principale includes a part of
584 the Rhaetian (Neri et al., 2007) and, thus, its upper boundary is near the Triassic-Jurassic
585 boundary at 201.3 Ma. The seawater curve was fixed at the lower boundary of the
586 Travenanzes Fm. and the time axis was varied to fit the seawater curve parallel to the
587 envelope of minimal $^{87}\text{Sr}/^{86}\text{Sr}$ -ratios measured in the dolomites (Fig. 10). The base of the first
588 massive dolomite at 110 m in the profile would then have an age of approximately 229 Ma.

589 Comparison with the seawater curve shows that the dolomites of the Travenanzes Fm. have
590 largely marine $^{87}\text{Sr}/^{86}\text{Sr}$ -ratios (Fig. 10). Only values from micro-drilled samples most gently
591 extracted with 0.1 N acetic acid were used for this reconstruction, and the resulting values all
592 lie within a range of 0.00022 with the seawater values (grey shaded area). This scatter
593 towards more positive values, compared to seawater, may be due to a small influence of



Sr-isotopes in Carnian primary dolomite

594 continental water. Indeed, during deposition of the Travenanzes Fm. sufficient continental
595 water would have been available from rivers, and ions may have become concentrated while
596 the water was evaporating in the distal alluvial plain. Alternatively, Sr desorbed from clay
597 minerals could have added more radiogenic values to the brine. But even if a small influence
598 of Sr of continental origin is present, because of the much higher Sr concentrations in
599 seawater, the marine signal is dominant.

600 This observation does not support the classical Coorong model for dolomite formation,
601 where alkalinity is largely derived from continental groundwater. The Coorong Lakes in
602 South Australia are ephemeral lakes largely supplied with groundwater (Von der Borch et al.,
603 1975). Strangely, though, the $^{87}\text{Sr}/^{86}\text{Sr}$ ratios we measured in Milne Lake (one of the Coorong
604 Lakes) show modern seawater composition (Fig. 11), but this can be explained as the local
605 groundwater largely originates from a Pleistocene carbonate aquifer, accordingly carrying a
606 Pleistocene Sr-isotope signature. A similar scenario for the Travenanzes Fm. is unlikely as the
607 only large-scale preceding carbonate platforms at that time were the Late Ladinian-Carnian
608 Cassian dolomite platforms (Russo et al., 1997). But based on the stratigraphic context, all
609 basins between these platforms were infilled by the Heiligkreuz Fm. and an extremely flat
610 topography had established that was stratigraphically overlain and sealed by the alluvial
611 deposits of the laterally persistent Travenanzes Formation. Furthermore, the Travenanzes Fm.
612 consists of 100 m of impermeable clay (containing expandable clays) such that a long-
613 distance transport of groundwater can be excluded.

614 We conclude that the $^{87}\text{Sr}/^{86}\text{Sr}$ ratios of the dolomites truly represent a dominating marine
615 influence. Presumably, seawater was transported to the interior of the platforms by episodic
616 flooding (spring tide or storm) events. Even in a seasonally wet climate the input of river
617 water on Sr-isotopes was insignificant compared to the influence of ions (including Sr) from
618 seawater that became concentrated by evaporation. Laminated dolomites in the uppermost
619 part of the section show values most similar to seawater composition, which is consistent with



Sr-isotopes in Carnian primary dolomite

620 a greater influence of peritidal conditions.

621

622 *The influence of Sr adsorbed to clay minerals*

623 An outlier with higher $^{87}\text{Sr}/^{86}\text{Sr}$ ratios occurs in a dolomite nodule, presumably representing
624 a more continental influence or perhaps more seasonally wet and evaporative conditions with
625 less marine influence. But also higher values may be due to contamination and partial
626 leaching of clay minerals within the dolomite samples. Within the extraction sequence (1 M
627 NaCl → 0.1 N acetic acid → 1 N acetic acid), the $^{87}\text{Sr}/^{86}\text{Sr}$ ratio generally remains constant or
628 becomes slightly less radiogenic, i.e., more similar to seawater. However, the values strongly
629 increase with leaching in 6 N HCl (Table 6). A modification of the $^{87}\text{Sr}/^{86}\text{Sr}$ ratios due to
630 contamination by ^{87}Sr from the radioactive decay of ^{87}Rb to ^{87}Sr can be considered as
631 negligible since the concentrations of Rb was below the detection limit of 0.05 ppm (Table 5)
632 and the half time of the decay is 48.8 billion years. Also, an influence of celestine and Sr-rich
633 barite, observed under the SEM, on the Sr-isotope values can be largely excluded. These
634 mineral phases are bound to distinct layers of the laminated dolomites, where they could be
635 avoided by micro-drilling in areas where the dolomite was pure. Only one value in sample
636 TZ14-9 shows extremely high Sr-concentrations. This sample was micro-drilled near to a
637 celestine layer and it is therefore not surprising that a celestine crystal may have been leached.
638 The isotopic composition of the celestine is also similar to Carnian seawater.

639 In the NaCl-fraction only minimal amounts of dolomite are dissolved. The slightly more
640 radiogenic $^{87}\text{Sr}/^{86}\text{Sr}$ ratio may be derived from Sr that is lightly adsorbed to clay minerals and
641 finely dispersed in the clay matrix, although Sr^{2+} as a two-valent cation is more strongly
642 adsorbed to clay mineral than Na^+ , and thus not easily desorbed by NaCl. With increasing
643 extraction efficiency and purity of the carbonate phase, the values approach seawater values
644 in the 1 N acetic acid fraction. Also, values from micro-drilled samples are generally more
645 similar to seawater values, probably because more pure dolomite was sampled (Table 6). 1 N



Sr-isotopes in Carnian primary dolomite

646 acetic acid is usually observed not to strongly attack interlayer ions in clay minerals.

647 Clay minerals leached in 6 N HCl show significantly more radiogenic values compared to
648 dolomite samples (Table 6). This finding is consistent with strongly radiogenic values in the 6
649 N HCl-fraction of dolomite samples (up to 0.730453 ± 0.000005) and supports that the clay
650 minerals are the carriers of a Sr-pool significantly more radiogenic than the carbonate phase
651 showing marine values. Sr is known to adsorb to illite-smectite mixed layer clay minerals
652 (Missana et al., 2008). The HCl-fraction most likely includes adsorbed Sr, and Sr occupying
653 the interlayer positions of the clay minerals, and presumably also structurally bound Sr in the
654 clay mineral phase. In particular, illite-smectite mixed-layer clay minerals, as detected by
655 XRD of the clay mineral separate in sample TZ14-9 (Fig. 7d), could have two different
656 origins, burial diagenesis and continental weathering. Based on the tectonic setting and low
657 burial depth of the Dolomites, burial depth for smectite-illite transition has not been reached.
658 Therefore, these minerals are most likely derived from silicate weathering, with the Sr-
659 signature representing the crustal origin of the parent rock. Our finding of radiogenic Sr-
660 isotope ratios supports that clay minerals did not essentially incorporate the Sr from seawater,
661 delivered at high sealevel stand. It is therefore clear that Sr extracted from the dolomites is not
662 derived from clay minerals.

663

664 *Dolomite as primary archive of Sr-isotope signatures*

665 The question is, whether Sr truly represents the conditions of dolomite formation or
666 whether it inherits the Sr content of some precursor phase. Baker and Burns (1985) and
667 Vahrenkamp and Swart (1990) showed very small distribution coefficients between aqueous
668 and solid solutions, and high Sr-contents measured in Abu Dahbi sabkha dolomites (Müller et
669 al., 1990b) may be derived from precursor aragonite. However, dolomite in the Travenanzes
670 Fm. is largely primary (Preto et al., 2015) and thus not formed from an aragonite precursor. It
671 is likely that remobilization of Sr during burial may have released parts of the Sr from



Sr-isotopes in Carnian primary dolomite

672 dolomite which is now present as celestine and barite inclusions.

673 Furthermore, Sánchez-Román et al. (2011) demonstrated that protodolomite forming in
674 culture experiments contain Sr in the range of several thousand ppm. The incorporation
675 mechanism of Sr is still not entirely clear, since Sr is a large ion that should occupy the sites
676 of Ca in the crystal lattice. However, in Sánchez-Román et al. (2011) Sr appears to correlate
677 with the Mg content, and another incorporation mechanism may occur, such as by surface
678 entrapment. A correlation of Sr-contents with K-contents is observed for the Travenanzas
679 dolomites. It could be circumstantial, but would not be inconsistent with an alternative
680 mechanism of Sr-incorporation, such as surface entrapment. Even if it is taken into account
681 that only protodolomite formed in microbial culture experiments (Gregg et al., 2015), natural
682 modern dolomites are often rich in Sr (e.g. Meister et al., 2007). The Sr could occur in
683 disordered nano-structural domains that are not picked up in the bulk XRD-signal.
684 Alternative, non-classical nucleation and growth pathways, e.g. by nano-particle attachment,
685 could play a role in the abnormal partitioning of Sr in the dolomite lattice. Thus, a high Sr-
686 content in the Travenanzas Fm. or in Abu Dhabi Sabkha dolomites is likely a true signature of
687 primary dolomites.

688

689 **5.3 Mode of dolomite formation and comparison with known models**

690 *Primary dolomite formation*

691 Several indications support that the origin of dolomite in the Travenanzas Fm. is largely
692 primary. Formation temperatures reconstructed from oxygen isotopes and assuming Triassic
693 seawater composition of -1‰ VSMOW are between 28 and 33°C. If a typical ¹⁸O enrichment
694 of 3‰ in a sabkha (McKenzie et al., 1980; McKenzie, 1981) is assumed, the calculated
695 temperatures would be between 40 and 50°C, which is still within a range possible in a
696 sabkha. Both temperature and evaporation may have changed over time, which may explain
697 the observed linear trend in oxygen isotopes across the section (Fig. 8B). Furthermore, there is



Sr-isotopes in Carnian primary dolomite

698 no co-variation between $\delta^{13}\text{C}$ and $\delta^{18}\text{O}$, as opposed to evaporation in hydrologically closed
699 settings such as the Germanic Keuper basin (Reinhardt and Ricken, 2000; Arp et al., 2005).
700 Both oxygen isotopes and nano-crystalline structures observed by Preto et al. (2015) preclude
701 a later pervasive recrystallization during burial diagenesis. Sedimentary structures indicate
702 that most of the homogenous dolomite and laminae containing aphanotopic dolomite was
703 unlithified, and dolomite was therefore deposited as fine-grained mud. This is further
704 supported by mm-scale interlayering of clay and dolomite in the laminated dolomites near the
705 top of the sequence, and some dolomite/clay couplets showing a fining-upward bedding.
706 Based on the observation of nano-crystal structures, replacement did not take place and it
707 appears logical to assume that the primary phase was already dolomite.

708 While most of the dolomite may have been primary, micron-scale interstices between the
709 dolomicrite grains must have been cemented after deposition. This cementation resulted in
710 rims visible under the SEM and resulting in near hexagonal compromise boundaries. The
711 cement may have contributed ^{13}C -depleted carbon during early diagenesis. The lowest $\delta^{13}\text{C}$
712 values of -3.4‰ VPDB occur in the nodules. There is no indication that these nodules formed
713 at the surface. They rather formed within the sediment, probably due to reducing conditions
714 and influenced by dissolved inorganic carbon from degrading organic matter in the
715 palaeosols. Homogeneous and laminated dolomites are clearly distinct from nodules in their
716 carbon isotope compositions (Fig. 8a), indicating only a minor contribution from pore-water
717 derived dissolved inorganic carbon. Carbon isotope values are thus largely consistent with a
718 primary precipitation. The mode of dolomite formation as fine mud and subsequent
719 cementation is comparable to several modern sites of dolomite formation.

720

721 *The sabkha model*

722 The classical sabkha model involves dolomite formation under intra-supratidal conditions,
723 concentration of brines through either seepage reflux (Adams and Rhodes, 1960) or



Sr-isotopes in Carnian primary dolomite

724 evaporative pumping (Hsü and Siegenthaler, 1969; Hsü and Schneider, 1973; McKenzie et
725 al., 1980; McKenzie, 1981) and precipitation of dolomite upon increase of the Mg/Ca ratio
726 due to gypsum precipitation (see Machel, 2004, for a more detailed discussion of varieties of
727 sabkha models). This group of models allow for a mixture of seawater and continental
728 groundwater, with seawater providing mainly the ions for dolomite precipitation. Coastal
729 sabkhas are typically characterized by laminated (Lofer-type) dolomites, whereby the laminae
730 are largely still unlithified after deposition (Illing, 1965; Bontognali et al., 2010; Court et al.,
731 2017). In fact, in the sabkha of Abu Dhabi, both pathways, via replacement of precursor
732 aragonite and by direct precipitation of dislocation-ridden primary dolomite, were observed
733 (Wenk et al., 1993).

734 The sabkha model is thus a reasonable model for the uppermost parts of the Travenanzes
735 section, showing laminated dolomites, marine Sr-isotope values and indications of frequent
736 desiccation and flooding in a peritidal setting. Yet, the conditions differed from the modern
737 sabkhas along the Persian Gulf by the large amount of alluvial clay (dirty sabkha), as opposed
738 to aeolian sand. Most of the fine lamination then may result from periodically varying
739 conditions, perhaps with clay deposition during episodes of fluvial discharge and carbonate
740 deposition during evaporative conditions.

741

742 *The continental playa lake model*

743 The playa lake model was originally suggested by Eugster and Surdam (1973) for dolomite
744 of the Green River Formation (Wyoming), but the primary formation of fine dolomite mud is
745 observed in many alkaline playa lakes, such as Deep Springs Lake (Peterson et al., 1963;
746 Clayton et al., 1968; Meister et al., 2011), Lake Acigöl (Turkey; Balci et al., 2017), Lake
747 Neusiedl (Austria; cf. Neuhuber et al., 2016), Lake Van (Turkey; McCormack et al., 2018; for
748 an overview see Eugster and Hardie, 1978, and Last, 1990). This type of setting has also been
749 suggested for the Germanic Keuper deposits during the late Carnian and Norian, when the



Sr-isotopes in Carnian primary dolomite

750 Germanic Basin was entirely disconnected from the Panthalassa ocean and was continental
751 (Reinhardt and Ricken, 2000). The Travenanzes Fm., with its homogeneous dolomite
752 intercalations in red and green clays, is strikingly similar to playa-lake Keuper facies in the
753 Germanic Basin. There, dolomite formed upon evaporation and concentration of the
754 continental brines under semi-arid climate.

755 However, Sr-isotope data support a dominantly marine origin of ionic solutions to the
756 Travenanzes Fm., whereas Sr-isotopes are strongly radiogenic in the Germanic Keuper
757 dolomites (or in Deep Springs Lake; Fig. 11). The two settings are thus fundamentally
758 different. Even dolomite nodules, showing somewhat more radiogenic values than seawater in
759 the Travenanzes Fm., are still indicating a dominating marine influence. The slightly more
760 radiogenic influence could be due to the clay minerals present in the nodules that were
761 difficult to entirely separate from the carbonate. Also, dolomite nodules may have formed in
762 relation to palaeosols, during somewhat more humid times and, thus, may have been slightly
763 influenced by continental water input from the rivers.

764

765 *The coastal ephemeral lake model (Coorong model)*

766 The Coorong model was proposed by Von der Borch et al., 1975; Von der Borch 1976;
767 Rosen et al., 1989; see Warren, 2000, for detailed information), explaining the formation of
768 primary and uncemented dolomite in the Coorong lakes of South Australia. The isotope
769 values show that the contribution of ionic solutions, and hence alkalinity, of continental origin
770 to the dolomitizing fluids was minimal and that the dolomites are seawater derived. This may
771 be distinct from the typical Coorong model, where alkalinity is provided from an inland karst
772 system. But other coastal ephemeral lakes exist, such as along the Brazilian coast north of Rio
773 de Janeiro. Partially unlithified dolomite occurs in Brejo do Espinho (Sánchez-Román et al.,
774 2009), which is in fact largely similar to the Coorong lakes, but ionic solutions are largely
775 derived from seawater.



Sr-isotopes in Carnian primary dolomite

776 A coastal ephemeral lake model would probably be most suitable to explain homogeneous
777 dolomite beds of the Travenanzes Fm., where hypersaline ponds may have formed in a
778 dryland river system. However, unlike the recent ephemeral lakes (such as Lagoa Vermelha,
779 Brejo do Espinho and the Coorong Lakes) the clay-rich sediment must have inhibited
780 groundwater flow. Hence, while modern coastal ephemeral lakes receive their water largely
781 through seawater percolating through porous dune sand, episodic flooding with seawater must
782 have provided ionic solutions for dolomite formation on the Carnian platform.

783

784 *A non-actualistic system*

785 Overall, the depositional environment reconstructed for the Travenanzes Fm. shows
786 similarities to modern systems where dolomite forms. Among all the scenarios, a coastal
787 ephemeral lake model would be most similar to the conditions conducive to homogeneous
788 dolomites, lacking signs of frequent desiccation, while a coastal sabkha model may explain
789 the laminated intervals near the top of the studied succession. In contrast to any modern
790 systems, the clay rich sediments of the Travenanzes Fm. precluded any transport of
791 groundwater, which plays a role for ionic transport in both the modern day ephemeral lake
792 model and the different versions of sabkha models. Although modern systems provide valid
793 analogues for the mechanism of dolomite formation in the past, and probably throughout
794 Earth's history, none of them is an exact environmental analogue. The Carnian alluvial plains
795 that covered an enormous area along the Tethys margin (e.g. Garzanti et al., 1995) represent a
796 non-actualistic system in terms of their sedimentary, hydrological and climatic conditions.
797 Besides, the geochemistry of Tethys seawater may also have been different from today, an
798 issue that requires further investigation. These aspects need to be taken into account if we
799 intend to understand the role of dolomite formation through Earth history.

800 In the light of a possible spontaneous precipitation as fine mud in the water column,
801 perhaps via formation and aggregation of nano-particles, further discussion of a nucleation



Sr-isotopes in Carnian primary dolomite

802 and growth pathway of dolomite will be necessary. While several modifiers may also play a
803 role in the water column, such as dissolved organic matter (Frisia et al., 2018), microbial EPS
804 (Bontognali et al., 2013), or suspended clay particles (Liu et al., 2018), fluctuating conditions
805 inducing spontaneous nucleation and growth of dolomite, in agreement with Ostwald's step
806 rule (Deelman, 1999), require further consideration as a factor favourable for dolomite
807 formation on a seasonally variable platform (Meister and Frisia, accepted).

808 The main finding of this study is that most of the dolomite in the >100 m thick
809 Travenanzes Fm. probably formed through direct precipitation in a seawater-derived solution.
810 This mode of primary dolomite formation has rarely been considered in the study of
811 geological dolomite bodies, but may explain the genesis of many other large-scale, fine
812 dolomite units that preserve fossils and sedimentary structures.

813

814 **6 Conclusions**

815 Dolomite beds intercalated in a 100-m-thick Carnian alluvial clay sequence in the
816 Travenanzes Fm. largely formed as fine-grained primary mud. The depositional environment
817 was minimally affected by currents and most likely prevailed as ephemeral lakes in an
818 extended alluvial plain or dryland river system. The large amounts of clay are related to at
819 least seasonally wet conditions. Also palaeosols and diagenetic dolomite nodules could have
820 formed under such conditions. The facies resembles strongly those of the Triassic playa lakes
821 prevailing in the Germanic Basin or in the modern Deep Springs Lake.

822 Sr-isotopes clearly show a marine signal, indicating seawater as the main source of ions.
823 The depositional environment shows most similarities with coastal ephemeral lakes resulting
824 in the deposition of homogeneous dolomite beds through most of the sequence, changing into
825 a "dirty" sabkha near the top of the sequence, where fine dolomite/clay interlayers suggest
826 alternating deposition of extremely fine authigenic dolomite from evaporating water, and
827 clay.



Sr-isotopes in Carnian primary dolomite

828 Overall, Sr-isotopes and petrographic observations provide insight into a non-
829 uniformitarian system including both elements of coastal ephemeral lake systems and sabkhas
830 as an environment of primary dolomite formation. Considering the precipitation of primary
831 dolomite from coastal lakes or ponds may help explaining other dolomite deposits with
832 preserved sedimentary features throughout geologic history.

833

834 *Acknowledgements.* We thank C. Beybel, I. Wünsche, and L. Slawek for preparing high-
835 quality petrographic thin sections. Thanks also to W. Obermaier for analysing element
836 concentrations by ICP-OES and P. Körner for support during TOC measurements. S.
837 Niebergall provided some of the petrographic images. We furthermore thank S. Viehmann for
838 help during sampling and supervision of the students in the field and B. Bethke for her strong
839 support in the laboratory. Thanks also to M. Lorecak for the help during sampling of
840 dolomite from the Coorong Lagoon. We thank S. Frisia for input and constructive criticism.
841 F. Franchi and H. Machel reviewed an early version of this manuscript. The study was
842 partially supported by the Marie Curie Intra-European Fellowship Project Triadol (Project no.
843 626025).

844

845 **References**

- 846 Adams, J.E., and Rhodes, M.L.: Dolomitization by seepage refluxion, Am. Assoc. Petrol.
847 Geol. Bull., 44, 1912–1921, 1960.
- 848 Alderman, A.R. and Skinner, H.C.W.: Dolomite sedimentation in the South-East of South
849 Australia, Am. J. Sci., 255, 561–567, 1957.
- 850 Arp, G., Hoffmann, V.-E., Seppelt, S., and Riegel, W.: Trias und Jura von Göttingen und
851 Umgebung, 74. Jahrestagung der Paläontologischen Gesellschaft, 2.-8.10.2004, Exkursion,
852 6, 147–192, Göttingen (Universitätsdrucke), 2004.



Sr-isotopes in Carnian primary dolomite

- 853 Arp, G., Bielert, F., Hoffmann, V.-E., and Löffler, T.: Palaeoenvironmental significance of
854 lacustrine stromatolites of the Arnstadt Formation (“Steinmergelkeuper”, Upper Triassic,
855 N-Germany), *Facies*, 51, 419–441, 2005.
- 856 Baker, P.A. and Burns, S.J.: Occurrence and formation of dolomite in organic-rich continental
857 margin sediments, *Am. Assoc. Petrol. Geol. Bull.*, 69, 1917–1930, 1985.
- 858 Balci, N., Menekşe, M., Karagüler, N.G., Sönmez, M.S., and Meister, P.: Reproducing
859 authigenic carbonate precipitation in the hypersaline Lake Acıgöl (Turkey) with microbial
860 cultures, *Geomicrobiology Journal*, 33, 758–773, 2016.
- 861 Bontognali, T.R.R., Vasconcelos, C., Warthmann, R.J., Bernasconi, S.M., Dupraz, C.,
862 Strohmenger, C.J., and McKenzie, J.A.: Dolomite formation within microbial mats in the
863 coastal sabkha of Abu Dhabi (United Arab Emirates), *Sedimentology*, 57, 824–844, 2010.
- 864 Bontognali T.R.R., McKenzie J.A., Warthmann R. and Vasconcelos C. (2013) Microbially
865 influenced formation of Mg-calcite and Ca-dolomite in the presence of exopolymeric
866 substances produced by sulphate-reducing bacteria. *Terra Nova*, 26, 72–77.
- 867 Bouton, A., Vennin, E., Pace, A., Bourillot, R., Dupraz, C., Thomazo, C., Brayard, A.,
868 Désaubliaux, G., and Visscher, P.T.: External controls on the distribution, fabrics and
869 mineralization of modern microbial mats in a coastal hypersaline lagoon, Cayo Coco
870 (Cuba), *Sedimentology*, 63, 972–1016, 2016.
- 871 Brack, P., Mundil, R., Oberli, F., Meier, M., and Rieber, H.: Biostratigraphic and radiometric
872 age data question the Milankovitch characteristics of the Latemar cycles (Southern Alps,
873 Italy), *Geology*, 24, 371–375, 1996.
- 874 Brack, P., Rieber, H., and Urlichs, M.: Pelagic successions in the Southern Alps and their
875 correlation with the Germanic Middle Triassic, *Zentralbl. Geol. Paläontol. Teil I*, 7–8,
876 853–876, 1999.



Sr-isotopes in Carnian primary dolomite

- 877 Breitenbach, S.F.M. and Bernasconi, S.M.: Carbon and oxygen isotope analysis of small
878 carbonate samples (20 to 100 μg) with a GasBench II preparation device, *Rapid Commun.*
879 *Mass Spectrom.*, 25, 1910–1914, 2011.
- 880 Burns, S.J., McKenzie, J.A., and Vasconcelos, C.: Dolomite formation and biogeochemical
881 cycles in the Phanerozoic, *Sedimentology*, 47, 49–61, 2000.
- 882 Breda, A. and Preto, N.: Anatomy of an Upper Triassic continental to marginal-marine
883 system: the mixed siliciclastic–carbonate Travenanzes Formation (Dolomites, Northern
884 Italy), *Sedimentology*, 58, 1613–1647, 2011.
- 885 Chilingar, G.V.: Relationship between Ca/Mg ratio and geological age, *AAPG Bull.*, 40,
886 2256–2266, 1956.
- 887 Clayton, R.N., Jones, B.F., and Berner, R.A.: Isotope studies of dolomite formation under
888 sedimentary conditions, *Geochim. Cosmochim. Acta*, 32, 415–432, 1968.
- 889 Cleveland, D.M., Nordt, L.C., and Atchley, S.C.: Paleosols, trace fossils, and precipitation
890 estimates of the uppermost Triassic strata in northern New Mexico. *Palaeogeography,*
891 *Palaeoclimatology, Palaeoecology*, 257, 421–444, 2008.
- 892 Court, W.M., Paul, A., and Lokier, S.W.: The preservation potential of environmentally
893 diagnostic sedimentary structures from a coastal sabkha, *Marine Geology*, 386, 1–18,
894 2017.
- 895 Czurda, K. and Nicklas, L.: Zur Mikrofazies und Mikrostratigraphie des Hauptdolomites und
896 des Plattenkalk-Niveaus der Klostertaler Alpen und des Rhätikon (Nördliche Kalkalpen,
897 Vorarlberg), In: *Festband 300 Jahre Geol. Inst. Univ. Innsbruck*, pp. 165–253, 1970.
- 898 Dal Corso, J., Mietto, P., Newton, R.J., Pancost, R.D., Preto, N., Roghi, G., and Wignall, P.B.
899 Discovery of a major negative $\delta^{13}\text{C}$ spike in the Carnian (Late Triassic) linked to the
900 eruption of Wrangellia flood basalts, *Geology*, 40, 79–82, 2012.
- 901 Deelman, J.C.: Low-temperature nucleation of magnesite and dolomite, *Neues Jahrbuch für*
902 *Mineralogie (Stuttgart), Monatshefte*, 7, 289–302, 1999.



Sr-isotopes in Carnian primary dolomite

- 903 Demicco, R.V. and Hardie, L.A.: Sedimentary structures and early diagenetic features of
904 shallow marine carbonate deposits, *SEPM Atlas, Ser.*, 1, 265, 1994.
- 905 DePaolo, D.J. and Ingram, B.: High-resolution stratigraphy with strontium isotopes. *Science*,
906 227, 938–941, 1985.
- 907 De Zanche, V., Gianolla, P., Mietto, P., Siorpaes, C., and Vail, P.R.: Triassic sequence
908 stratigraphy in the Dolomites (Italy), *Sci. Geol. Mem.*, 45, 1–27, 1993.
- 909 Doglioni, C.: Tectonics of the Dolomites (Southern Alps-Northern Italy), *J. Structural*
910 *Geology*, 9, 181–193, 1987.
- 911 Eugster, H.P. and Hardie, L.A.: Saline lakes, In: A. Lerman (Ed): *Lakes, Chemistry, Geology,*
912 *Physics*. Springer-Verlag, New York, N.Y., pp. 237-293, 1978.
- 913 Eugster, H.P. and Surdam, R.C.: Depositional environment of the Green River Formation of
914 Wyoming: a preliminary report, *Bull. Geol. Soc. Am.*, 84, 1115-1120, 1973.
- 915 Fischer, A.G.: The Lofer cyclothems of the Alpine Triassic, *Kansas Geol. Surv. Bull.* 169,
916 107–149, 1964.
- 917 Flügel, E.: *Microfacies of carbonate rocks - analysis, interpretation and application*, 2nd.
918 Edition, Springer-Verlag Berlin Heidelberg, 2010.
- 919 Frisia, S.: Mechanisms of complete dolomitization in a carbonate shelf: comparison between
920 the Norian Dolomia Principale (Italy) and the Holocene of Abu Dhabi Sabkha, In: A
921 volume in honour of Dolomieu (Eds: B. Purser, M. Tucker, and D. Zenger), *Spec. Publs.*
922 *Int. Ass. Sediment.*, 21, 55-74, 1994.
- 923 Frisia, S. and Wenk, H.-R.: TEM and AEM study of pervasive, multi-step dolomitization of
924 the upper Triassic Dolomia Principale (Northern Italy), *J. Sed. Petrol.*, 63, 1049–1058,
925 1993.
- 926 Füchtbauer, H. and Goldschmidt, H.: Beziehungen zwischen Calcium-Gehalt und
927 Bildungsbedingungen der Dolomite, *Geologische Rundschau*, 55, 29–40, 1966.



Sr-isotopes in Carnian primary dolomite

- 928 Gattolin, G., Breda, A., and Preto, N.: Demise of Late Triassic carbonate platforms triggered
929 the onset of a tide-dominated depositional system in the Dolomites, Northern Italy,
930 *Sedimentary Geology*, 297, 38–49, 2013.
- 931 Gattolin, G., Preto, N., Breda, A., Franceschi, M., Isottona, M., and Gianolla P.: Sequence
932 stratigraphy after the demise of a high-relief carbonate platform (Carnian of the
933 Dolomites): Sea-level and climate disentangled, *Palaeogeogr., Palaeoclimatol., Palaeoecol.*
934 423, 1–17, 2015.
- 935 Garzanti, E., Gnaccolini, M., and Jadoul, F.: Anatomy of a semiarid coastal system: the Upper
936 Carnian of Lombardy (Italy), *Riv. Ital. Paleontol. Stratigr.*, 101, 17–36, 1995.
- 937 Gianolla, P., De Zanche, V., and Mietto, P.: Triassic sequence stratigraphy in the Southern
938 Alps (Northern Italy): definition of sequences and basin evolution, In: *Mesozoic and*
939 *Cenozoic Sequence Stratigraphy of European Basins* (Eds. deGraciansky P.-C., J.
940 Hardenbol, T. Jacquin and P.R. Vail), *SEPM Spec. Publ.*, 60, 719–747, 1998.
- 941 Ginsburg, R.N.: Landward movement of carbonate mud: new model for regressive cycles in
942 carbonates (abs.), *AAPG Bull.*, 55, 340, 1971.
- 943 Given, R.K. and Wilkinson, B.H.: Dolomite abundance and stratigraphic age: constraints on
944 rates and mechanisms of Phanerozoic dolostone formation: perspectives, *J. Sediment.*
945 *Research*, 57, 1068–1078, 1987.
- 946 Gregg, J.M., Bish, D.L., Kaczmarek, S.E., and Machel, H.G.: Mineralogy, nucleation and
947 growth of dolomite in the laboratory and sedimentary environment: A review,
948 *Sedimentology* 62, 1749–1769, 2015.
- 949 Handy, M.R., Schmid, S.S., Bousquet, R., Kissling E., and Bernoulli, D.: Recoiling plate-
950 tectonic reconstructions of Alpine Tethys with the geological-geophysical record of
951 spreading and subduction in the Alps, *Earth-Science Reviews* 102, 121–158, 2010.
- 952 Hill, Jr., W.E., and Evans, D.R.: Solubility of twenty minerals in selected versene (EDTA)
953 solutions. State Geological Survey Kansas, *Bull.* 175, pp. 22, 1965.



Sr-isotopes in Carnian primary dolomite

- 954 Hsü, K.J. and Siegenthaler, C.: Preliminary experiments on hydrodynamic movement induced
955 by evaporation and their bearing on the dolomite problem, *Sedimentology*, 12, 11–25,
956 1969.
- 957 Hsü, K.J. and Schneider, J.: Progress report on dolomitization hydrology of Abu Dhabi
958 Sabkhas, Arabian Gulf, The Persian Gulf. Springer, New York, pp. 409–422, 1973.
- 959 Iannace, A. and Frisia, S.: Changing dolomitization styles from Norian to Rhaetian in
960 southern Tethys realm, In: A Volume in Honour of Dolomieu (Eds. B. Purser, M. Tucker
961 and D. Zenger), *Int. Assoc. Sedimentol. Spec. Publ.*, 21, 75–89, 1994.
- 962 Illing, L.V., Wells, A.J. and Taylor, J.C.M.: Penecontemporary dolomite in the Persian Gulf,
963 In: *Dolomitization and limestone diagenesis* (Eds L.C. Pray and L.C. Murray), *SEPM*
964 *Spec. Publ.*, 13, 89–111, 1965.
- 965 Jones, B.F.: The hydrology and mineralogy of Deep Springs Lake, Inyo County, California,
966 *US Geol. Surv. Prof. Paper*, 502-A, 56, 1965.
- 967 Korte, C., Kozur, H.W., Bruckschen, P., and Veizer, J.: Strontium isotope evolution of Late
968 Permian and Triassic seawater, *Geochim. Cosmochim. Acta* 67, 47–62, 2003.
- 969 Kraus, O.: Die Raibler Schichten des Drauzuges (Südliche Kalkalpen), *Lithofazielle,*
970 *sedimentpetrographische und paläogeographische Untersuchungen. Jb. Geol. B.-A.*, 112,
971 81–152, 1969.
- 972 Land, L.S.: Failure to precipitate dolomite at 25°C from dilute solution despite 1000-fold
973 oversaturation after 32 years, *Aquat. Geochem.*, 4, 361–368, 1998.
- 974 Last, W.M.: Lacustrine dolomite – an overview of modern, Holocene, and Pleistocene
975 occurrences, *Earth-Science Reviews*, 27, 221–263, 1990.
- 976 Liu, D., Xu, Y., Papineau, D., Yub, N., Fan, Q., Qiu, X., and Wang, H.: Experimental
977 evidence for abiotic formation of low-temperature proto-dolomite facilitated by clay
978 minerals, *Geochim. Cosmochim. Acta*, 247, 83–95, 2019.



Sr-isotopes in Carnian primary dolomite

- 979 Lumsden, D.N.: Discrepancy between thin-section and X-ray estimates of dolomite in
980 limestone, *J. Sed. Petrol.*, 49, 429–435, 1979.
- 981 Machel, H.G.: Concepts and models of dolomitization: a critical reappraisal. Geological
982 Society, London, Special Publications, 235, 7–63, 2004.
- 983 Mather, C.C., Skrzypek, G., Dogramaci, S., and Grierson, P.F.: Paleoenvironmental and
984 paleohydrochemical conditions of dolomite formation within a saline wetland in arid
985 northwest Australia, *Quaternary Science Reviews*, 185, 172–188, 2018.
- 986 McArthur, J.M., Howarth, R.J., and Shield, G.A.: Strontium isotope stratigraphy. The
987 geologic time scale, 2012, In: Gradstein, F.M., Ogg, J.G., Schmotz, M.D. and Ogg, G.M.
988 (eds.), Elsevier, 1 of 2, 1144 pp, 2012.
- 989 McCormack, J., Bontognali, T.R.R., Immenhauser, A., and Kwiecien, O.: Controls on cyclic
990 formation of Quaternary early diagenetic dolomite, *Geophysical Research Letters*, 45,
991 3625–3634, 2018.
- 992 McKenzie, J.: Holocene dolomitization of calcium carbonate sediments from the coastal
993 sabkhas of Abu Dhabi, U.A.E.. *J. Geol.*, 89, 185–198, 1981.
- 994 McKenzie, J., Hsü, K.J., and Schneider, J.F.: Movement of subsurface waters under the
995 sabkha, Abu Dhabi, UAE and its relation to evaporative dolomite genesis. *Spec. Publ.-*
996 *SEPM*, 28, 11–30, 1980.
- 997 Meister, P., Bernasconi, S., McKenzie, J.A., Vasconcelos, C., Frank, M., Gutjahr, M., and
998 Schrag, D., Dolomite formation in the dynamic deep biosphere: Results from the Peru
999 Margin (ODP Leg 201), *Sedimentology*, 54, 1007–1032, 2007.
- 1000 Meister, P., Reyes, C., Beaumont, W., Rincon, M., Collins, L., Berelson, W., Stott, L.,
1001 Corsetti, F., and Neelson, K.H.: Calcium- and magnesium-limited dolomite precipitation at
1002 Deep Springs Lake, California, *Sedimentology*, 58, 1810–1830, 2011.
- 1003 Meister, P., McKenzie, J.A., Bernasconi, S.M., and Brack, P.: Dolomite formation in the
1004 shallow seas of the Alpine Triassic, *Sedimentology*, 60, 270–291, 2013.



Sr-isotopes in Carnian primary dolomite

- 1005 Meister, P., Frisia, S.: Dolomite formation by nano-crystal aggregation in the Dolomia
1006 Principale of the Brenta Dolomites (northern Italy). *Rivista Italiana di Stratigrafia e*
1007 *Paleontologia*, under revision.
- 1008 Missana, T., Garcia-Gutierrez, M., and Alonso, U.: Sorption of strontium onto illite/smectite
1009 mixed clays, *Physics and Chemistry of the Earth*, 33, 156–162, 2008.
- 1010 Moore, D.M. and Reynolds, R.C.: *X-ray diffraction and the identification and analysis of clay*
1011 *minerals*, Oxford University Press, New York, 378 p, 1997.
- 1012 Müller, D.W., Mueller, P.A., and McKenzie, J.A.: Strontium isotopic ratios as fluid tracers in
1013 Messinian evaporites of the Tyrrhenian Sea (western Mediterranean Sea), In: Kastens,
1014 K.A., Mascle, J., et al., *Proc. ODP, Sci. Results, 107: College Station, TX (Ocean Drilling*
1015 *Program)*, 603–614, 1990a.
- 1016 Müller, D.W., McKenzie, J.A., and Mueller, P.A.: Abu Dhabi sabkha, Persian Gulf, revisited:
1017 application of strontium isotopes to test an early dolomitization model, *Geology*, 18, 618–
1018 621, 1990b.
- 1019 Muttoni, G., Kent, D.V., Garzanti, E., Brack, P., Abrahamsen, N., and Gaetani, M.: Early
1020 Permian Pangea ‘B’ to Late Permian Pangea ‘A’, *Earth Planet. Sci. Lett.*, 215, 379–394,
1021 2003.
- 1022 Neri, C., Gianolla, P., Furlanis, S., Caputo, R., and Bosellini, A.: Note illustrative della Carta
1023 Geologica d'Italia alla scala 1:50.000, Foglio 029 Cortina d'Ampezzo, A.P.A.T. System
1024 Cart, Roma, 200 pp, 2007.
- 1025 Neuhuber, S., Steier, P., Gier, S., Draganits, E., and Kogelbauer, I.: Radiogenic Carbon
1026 Isotopes in Authigenic Carbonate from Lake Neusiedl, Austria, *Geophysical Research*
1027 *Abstracts*, 17, 15399–15399, 2015.
- 1028 Ogg, J.G.: Triassic, In: Gradstein, F. M., Ogg, J. G., Schmitz, M., and Ogg, G. (Eds.), *The*
1029 *geologic time scale 2012*, Elsevier, Cambridge University Press, Cambridge, 681–730,
1030 2012.



Sr-isotopes in Carnian primary dolomite

- 1031 Perri, E., Tucker, M.E., Słowakiewicz, M., Whitaker, F., Bowen, L., and Perrotta, I.D.:
1032 Carbonate and silicate biomineralization in a hypersaline microbial mat (Mesaieed sabkha,
1033 Qatar): Roles of bacteria, extracellular polymeric substances and viruses, *Sedimentology*,
1034 65, 1213–1245, 2018.
- 1035 Peterson, M.N.A., Bien, G.S., and Berner, R.A.: Radiocarbon studies of recent dolomite from
1036 Deep Springs Lake, California. *J. Geophys. Res.*, 68, 6493–6505, 1963.
- 1037 Preto, N. and Hinnov, L.A.: Unravelling the origin of shallow-water cyclothem in the Upper
1038 Triassic Dürrenstein Formation (Dolomites, Italy). *J. Sed. Res.*, 73, 774–789, 2003.
- 1039 Preto, N., Breda, A., Corso, J. D., Spötl, C., Zorzi, F., and Frisia, S.: Primary dolomite in the
1040 Late Triassic Travenanzes Formation, dolomites, Northern Italy: facies control and
1041 possible bacterial influence, *Sedimentology*, 62, 697–716, 2015.
- 1042 Randazzo, A.F. and Zachos, L.G.: Classification and description of dolomitic fabrics of rocks
1043 from the Floridan aquifer, U.S.A. *Sediment. Geol.*, 37, 151–162, 1983.
- 1044 Ratschbacher, L., Merle, O., Davy, P., and Cobbold, P.: Lateral extrusion in the Eastern Alps,
1045 Part 1: Boundary conditions and experiments scaled for gravity, *Tectonics*, 10, 245–256,
1046 1991.
- 1047 Reinhardt, L. and Ricken, W.: The stratigraphic and geochemical record of Playa Cycles:
1048 monitoring a Pangaeian monsoon-like system (Triassic, Middle Keuper, S. Germany),
1049 *Palaeogeogr., Palaeoclimatol., Palaeoecol.*, 161, 205–227, 2000.
- 1050 Rodriguez-Blanco, J.D., Shaw, S., and Benning, L.G.: A route for the direct crystallization of
1051 dolomite, *American Mineralogist*, 100, 1172–1181, 2015.
- 1052 Rosen, M.R., Miser, D.E., Starcher, M.A., and Warren, J.K.: Formation of dolomite in the
1053 Coorong region, South Australia, *Geochim. Cosmochim. Acta*, 53, 661–669, 1989.
- 1054 Rosenbaum J. and Sheppard S.M.: An isotopic study of siderites, dolomites and ankerites at
1055 high temperatures, *Geochim. Cosmochim. Acta* 50, 1147–1150, 1986.



Sr-isotopes in Carnian primary dolomite

- 1056 Russo, F., Neri, C., Mastandrea, A., and Baracca, A.: The mud mound nature of the Cassian
1057 Platform Margins of the Dolomites A case history: the Cipit boulders from Punta
1058 Grohmann (Sasso Piatto Massif, northern Italy), *Facies*, 36, 25–36, 1997.
- 1059 Sánchez-Román, M., Vasconcelos, C., Warthmann, R., Rivadeneyra, M.A., and McKenzie,
1060 J.A.: Microbial dolomite precipitation under aerobic conditions: results from Brejo do
1061 Espinho Lagoon (Brazil) and culture experiments, *Int. Assoc. Sediment. Spec. Publ.*, 40,
1062 167–178, 2009.
- 1063 Sánchez-Román, M., McKenzie, J.A., Rebello Wagener, A., Romanek, C.S., Sánchez-Navas,
1064 A., and Vasconcelos, C.: Experimentally determined biomediated Sr partition coefficient
1065 for dolomite: Significance and implication for natural dolomite, *Geochim. Cosmochim.*
1066 *Ac.*, 75, 887–904, 2011.
- 1067 Seegis, D.: Die Lehrbergschichten im Mittleren Keuper von Süddeutschland: Stratigraphie,
1068 Petrographie, Paläontologie, Genese, Hennecke, Remshalden, 382 pp, 1997.
- 1069 Stampfli, G.M. and Borel, G.D.: A plate tectonic model for the Paleozoic and Mesozoic
1070 constrained by dynamic plate boundaries and restored synthetic oceanic isochrons, *Earth*
1071 *Planet. Sci. Lett.*, 196, 17–33, 2002.
- 1072 Teal, C.S., Mazzullo, S.J., and Bischoff, W.D.: Dolomitization of Holocene shallow-marine
1073 deposits mediated by sulfate reduction and methanogenesis in normal-salinity seawater,
1074 northern Belize, *J. Sediment. Research*, 70, 649–663, 2000.
- 1075 Vahrenkamp, V.C. and Swart, P.K.: New distribution coefficient for the incorporation of
1076 strontium into dolomite and its implications for the formation of ancient dolomites,
1077 *Geology*, 18, 387–391, 1990.
- 1078 Van Tuyl, F.M.: The origin of dolomite, Annual Report 1914, Iowa Geological Survey, XXV,
1079 257–421, 1914.



Sr-isotopes in Carnian primary dolomite

- 1080 Vasconcelos, C., McKenzie, J.A., Warthmann, R., and Bernasconi, S.: Calibration of the $\delta^{18}\text{O}$
1081 paleo-thermometer with dolomite formed in microbial cultures and natural environments.
1082 *Geology*, 33, 317–320, 2005.
- 1083 Vasconcelos, C., Warthmann, R., McKenzie, J.A., Visscher, P.T., Bittermann, A.G., and van
1084 Lith, Y.: Lithifying microbial mats in Lagoa Vermelha, Brazil: Modern Precambrian
1085 relics? *Sedimentary Geology*, 185, 175–183, 2006.
- 1086 Veizer, J., Ala, D., Azmy, K., Bruckschen, P., Buhl, D., Bruhn, F., Carden, G.A.F., Diener,
1087 A., Ebner, S., Godderis, Y., Jasper, T., Korte, C., Pawellek, F., Podlaha, O.G., and
1088 Strauss, H.: $^{87}\text{Sr}/^{86}\text{Sr}$, $\delta^{13}\text{C}$ and $\delta^{18}\text{O}$ evolution of Phanerozoic seawater, *Chemical geology*,
1089 161, 59–88, 1999.
- 1090 Von der Borch, C.C.: Stratigraphy and formation of Holocene dolomitic carbonate deposits of
1091 the Coorong area, South Australia, *J. Sediment. Research*, 46, 952–966, 1976.
- 1092 Von der Borch, C.C., Lock, D.E., and Schwebel, D.: Ground-water formation of dolomite in
1093 the Coorong region of South Australia, *Geology*, 3, 283–285, 1975.
- 1094 Warren, J.: Sedimentology and mineralogy of dolomitic Coorong Lakes, South Australia, *J.*
1095 *Sedimentary Petrol.*, 60, 843–858, 1990.
- 1096 Warren, J.: Dolomite: occurrence, evolution and economically important associations, *Earth-*
1097 *Science Reviews*, 52, 1–81, 2000.
- 1098 Wenk, H.R., Meisheng, H., and Frisia, S.: Partially disordered dolomite: microstructural
1099 characterization of Abu Dhabi sabkha carbonates, *Am. Mineral.*, 78, 769–774, 1993.

1100

1101 **Figure Captions**

1102 **Figure 1. (a)** Palaeogeographic map of the Southern Alpine to Germanic domains during the
1103 middle Triassic, reproduced from Brack et al. (1999; modified). Bal: Balaton; BG: Burgundy
1104 Gate; Car: Carnian Alps; ECG: eastern Carpathian Gate; Lomb: Lombardy; NCA: Northern
1105 Calcareous Alps; SMG: Silesian Moravian Gate. Inset: Tectonic map of the Southern Alps



Sr-isotopes in Carnian primary dolomite

1106 (Brack et al., 1996, modified) showing the sampling location at Rifugio Dibona. GL:
1107 Giudicarie Line; PL: Pustertal Line; VL: Val Sugana Line. **(b)** Stratigraphy of the middle to
1108 late Triassic in Venetian Alps, showing a transition in geometries from basin and platform
1109 topography during the Lower Carnian to an extended alluvial to tidal plain in this Upper
1110 Carnian. The shaded area indicates the Travenanzes Fm., showing a lateral transition in facies
1111 and a transgressive boundary to the Dolomia Principale. Compiled from Breda and Preto
1112 (2011), after De Zanche et al. (1993), modified.

1113

1114 **Figure 2.** Stratigraphic section at Rifugio Dibona: **(a)** Complete section modified after Breda
1115 and Preto (2011); **(a)** detailed section of uppermost part of the clay-rich interval, showing
1116 sampling locations. **(c)** Outcrop photograph showing the uppermost grey part of the clay-rich
1117 interval with the location of the profile shown in (b).

1118

1119 **Figure 3.** Outcrop images of different types of dolomite intercalated in red and grey clay of
1120 the Travenanzes Fm. at Rifugio Dibona: **(a)** Homogeneous dolomite bed (15 cm thick; 33 m).
1121 **(b)** Upper part: dolomite nodules embedded in red clay, crosscut by green coloured cracks as
1122 part of a calcic vertisol (95 m). **(c)** Laminated dolomite (110-112 m) in grey clay. **(d)** Bed
1123 with gypsum nodules, and cracks filled with gypsum, at 50 m; **(e)** Dolomite-cemented
1124 conglomerate bed at 75 m. **(f)** Laminated bed showing soft sediment deformation (106 m); an
1125 isoclinal synsedimentary fold is indicated by the arrow. **(g)** Laminated dolomite showing
1126 folding of the laminae due to soft sediment deformation (same bed as in f).

1127

1128 **Figure 4.** Photomicrographs of thin sections of dolomites of the Travenanzes Fm.: **(a)**
1129 Rounded mud clasts embedded in dolomicrite matrix. The larger mm-size intraclast in the
1130 upper left side of the image (arrow) consists itself of matrix with darker embedded mudclasts
1131 (sample TZ16-St1; 104 m). **(b)** Mud clasts in dolomicrite matrix. Mudclasts are deformed and



Sr-isotopes in Carnian primary dolomite

1132 layers of coarser and finer matrix are equally affected by plastic deformation (sample TZ16-
1133 22; 120 m). (c, d) Pseudomorphs after gypsum in fine-grained dolomudstone (arrows). (e)
1134 Oolitic grainstone (sample TZ14-4; 64 m). The cortices consist of microcrystalline dolomite
1135 lacking a radial structure. Some show a concentric structure (arrow). (f) Laminated dolomite
1136 showing pseudo-teepee structures (arrow). Vertical cracks are often, but not always,
1137 associated with pseudo-teepees (sample TZ14-10; 107 m). Some coarser grained laminae may
1138 contain microsparite and peloids (P). (g) Laminated dolomite showing both plastic and brittle
1139 deformation of laminae. A cm-scale pseudo-teepee occurs in the centre of the image (sample
1140 TZ 16-21; 107 m). (h, i) Closeup of graded lamina in (g) showing plastic deformation. The
1141 top of the lamina shows an erosion surface with small rip-up clasts (arrow), overlain by a
1142 coarser layer.

1143

1144 **Figure 5.** SEM images of dolomites in backscatter mode: (a) Overview showing layer
1145 enriched in celestine inclusions (bright areas) in dolomite (Sample TZ14-9d; 95 m); (b)
1146 Celestine inclusion with barite in the centre (same sample as in a); (c) Barite crystals in
1147 dolomicrite (sample TZ14-4; 65 m).

1148

1149 **Figure 6.** SEM images of dolomites in backscatter mode showing different types of crystal
1150 shape: (a) Spheroidal growth of dolomite (darker areas) in clay layers (brighter areas; sample
1151 TZ14-9d; 95 m). (b) Closeup of a. (c) Dolomite crystals showing a porous interior domain but
1152 homogeneous syntaxial cement rims (sample TZ14-12; 90 m). (d) Similar as in (c); sample
1153 TZ14-9d; 95 m).

1154

1155 **Figure 7.** X-ray diffraction patterns: (a) Bulk analyses of homogeneous dolomite (Samples
1156 TZ14-1, TZ14-7, and TZ14-9); main peaks and ordering peaks are labelled with (hkl) indices.
1157 (b-d) Clay mineral separates of samples TZ14-1, TZ14-7 and TZ14-9, air dried (N), saturated



Sr-isotopes in Carnian primary dolomite

1158 with ethylene glycol (EG), and heated to 550°C (T); d-values in Å. In the ethylene-glycol
1159 saturated sample TZ14-9 the illite-smectite mixed-layer is best seen. The arrow points at the
1160 expandable (smectite) part of the mixed-layer.

1161

1162 **Figure 8.** (a) Carbon/oxygen isotope cross-plot. (b) Oxygen isotope values through the
1163 stratigraphic section.

1164

1165 **Figure 9.** Element concentrations in sequentially extracted fractions of bulk dolomite and
1166 clay samples of the Travenanzes Fm.: (a) Ca vs. Mg; (b) Sr vs. K.

1167

1168 **Figure 10.** Comparison of Sr-isotopes in dolomites of the Travenanzes Fm. with Carnian
1169 seawater curve (Korte et al., 2003). The 2-sigma uncertainties are smaller than the symbol
1170 size.

1171

1172 **Figure 11.** Sr-isotope values from dolomites of different modern and ancient environments:
1173 Travenanzes Fm. in the Dolomites, Southern Alps; Germanic Keuper (Weser Formation and
1174 Arnstadt Formation); Coorong Lagoon; Deep Springs Lake. $^{87}\text{Sr}/^{86}\text{Sr}$ ratios of modern
1175 seawater are from DePaolo and Ingram (1985).

1176

TABLES

1178 **Table 1.** Compilation of sedimentary structures from thin section analysis of dolomites from
1179 the Travenanzes Fm. at the Dibona section.

1180

1181 **Table 2.** Relative abundances and ordering parameters of dolomites from the Travenanzes
1182 Formation. Relative abundances were estimated based on the 104 peak height. The
1183 stoichiometry $\text{Mg}/(\text{Ca}+\text{Mg})$ was determined from the shift of the 104 peak using the equation



Sr-isotopes in Carnian primary dolomite

1184 of Lumsden (1979). The structural ordering was calculated from the ratio of the 015 ordering
1185 peak to the 110 peak according to Füchtbauer and Goldschmidt (1966).

1186

1187 **Table 3.** Total inorganic and organic carbon (TIC, TOC) contents of clay samples from the
1188 Travenanzes Formation.

1189

1190 **Table 4.** Carbon and oxygen isotope values of different types of dolomite from the
1191 Travenanzes Formation.

1192

1193 **Table 5.** Element concentrations of leacheates from dolomites and clays used for Sr-isotope
1194 analysis.

1195

1196 **Table 6.** Compiled $^{87}\text{Sr}/^{86}\text{Sr}$ ratios of sequentially leached dolomites from different locations,
1197 clays and test minerals using different extraction solutions.

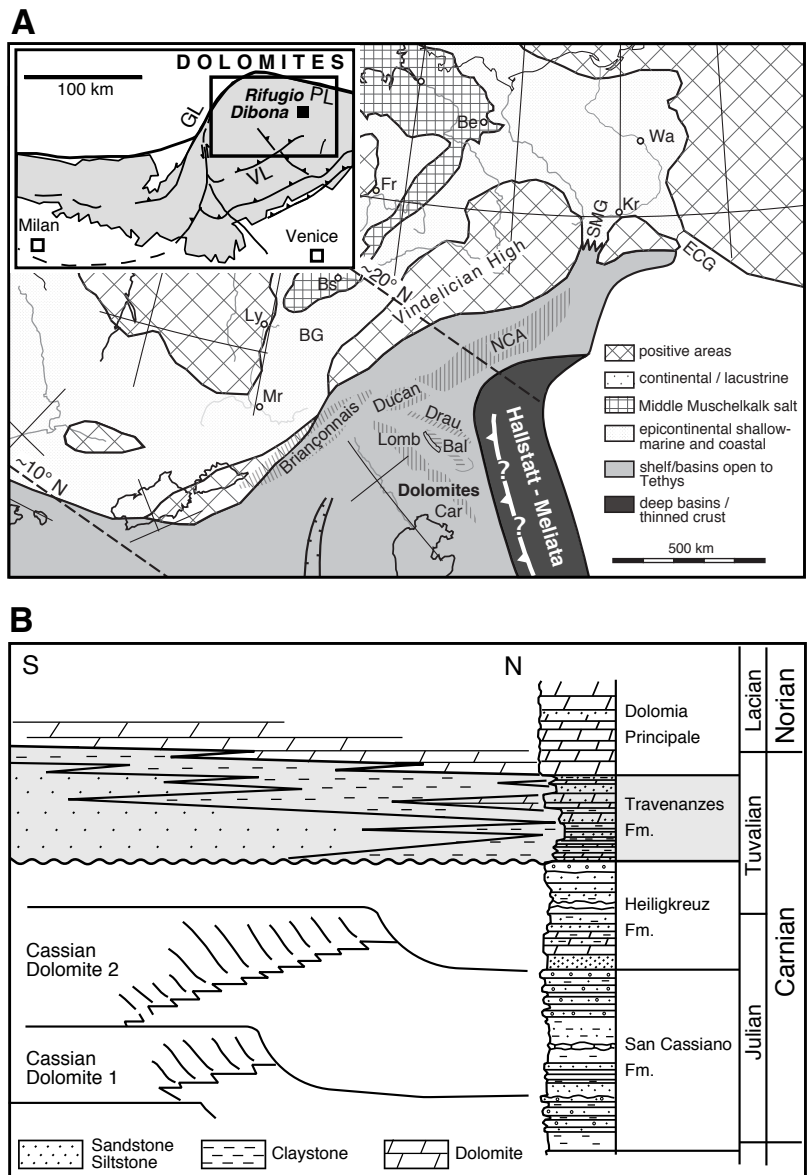


Figure 1

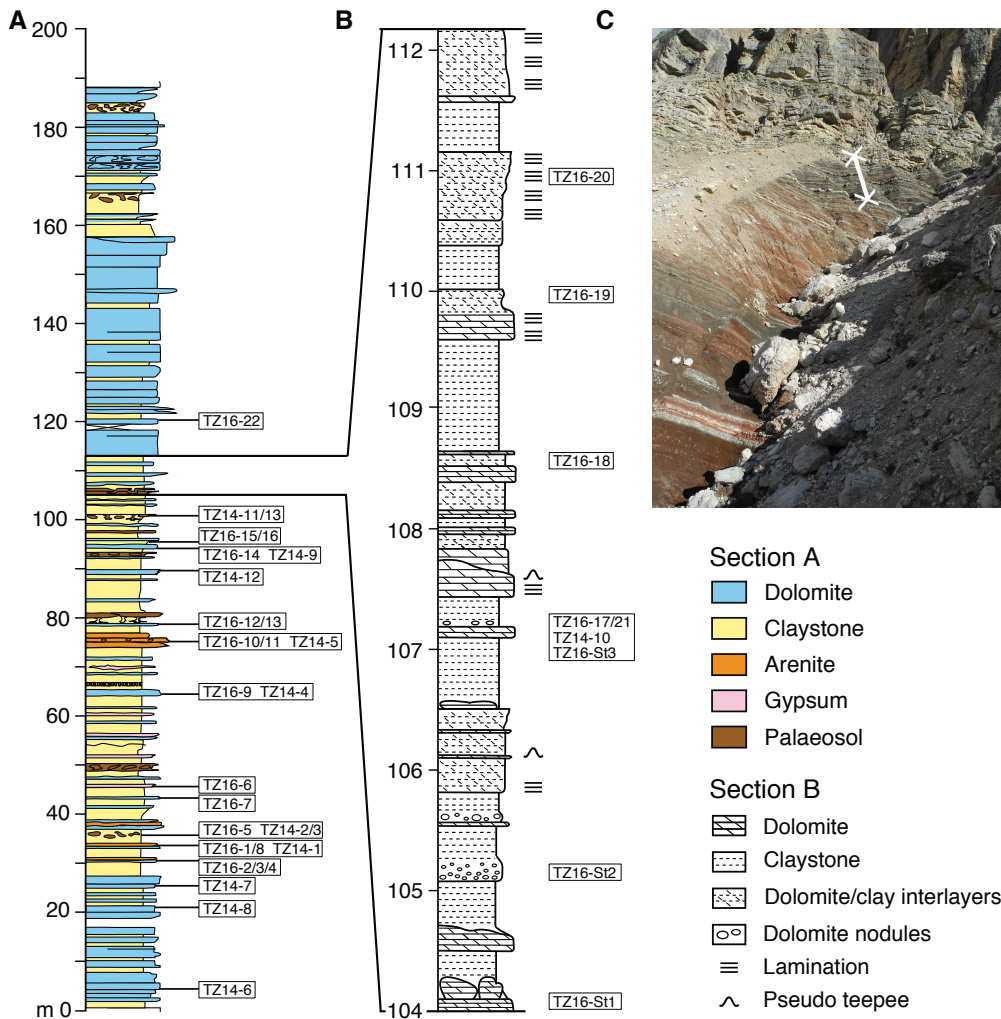


Figure 2

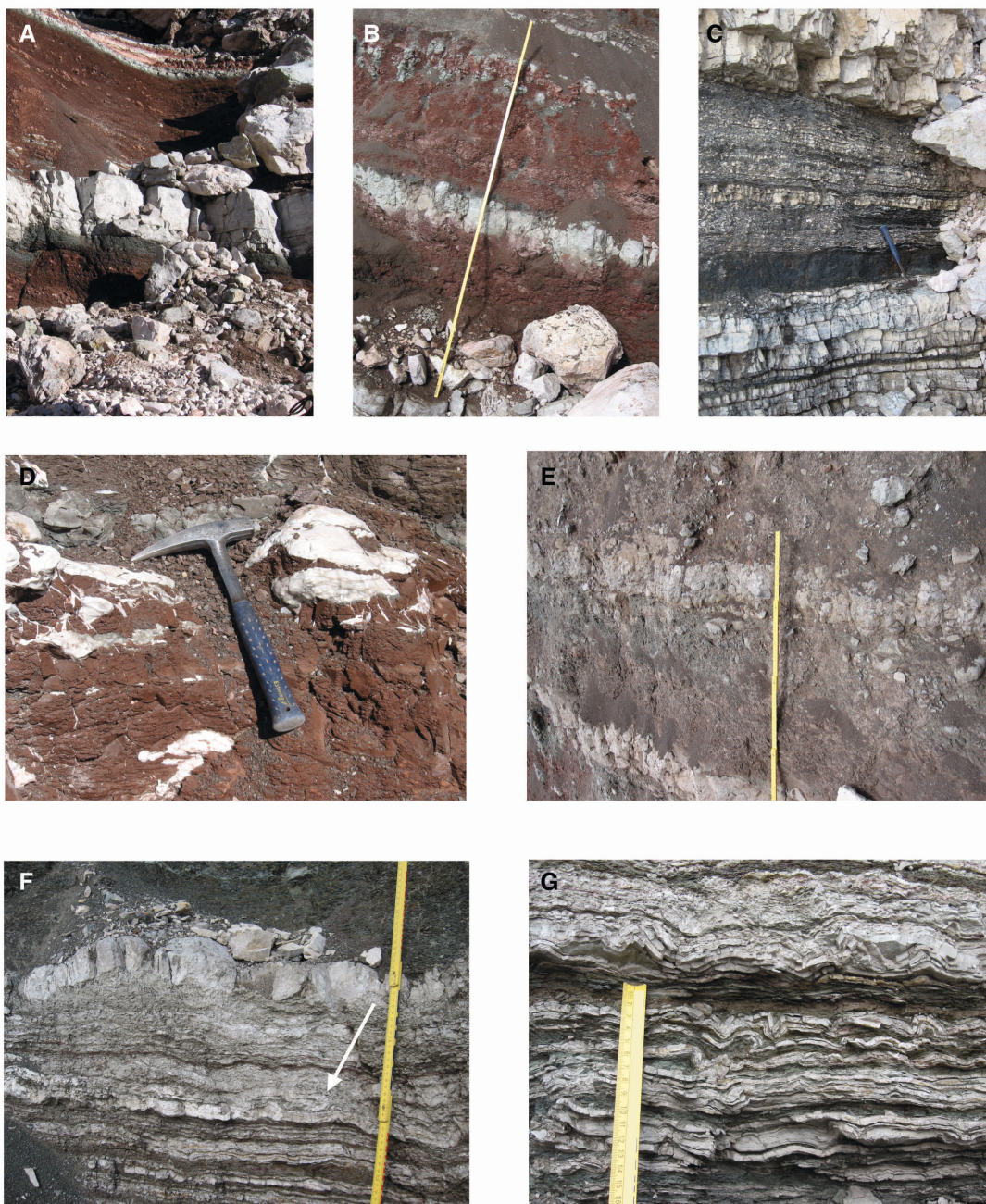


Figure 3

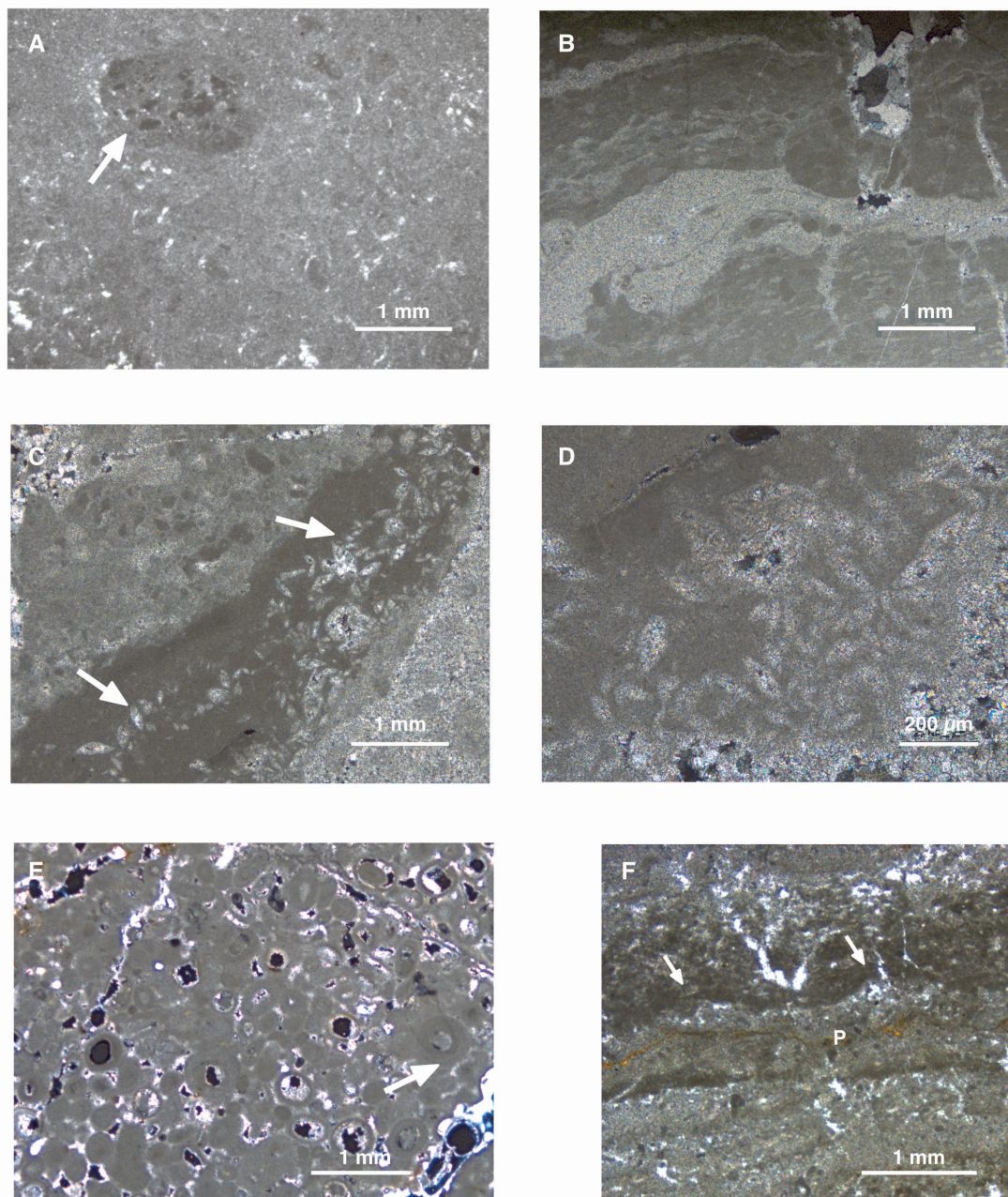


Figure 4

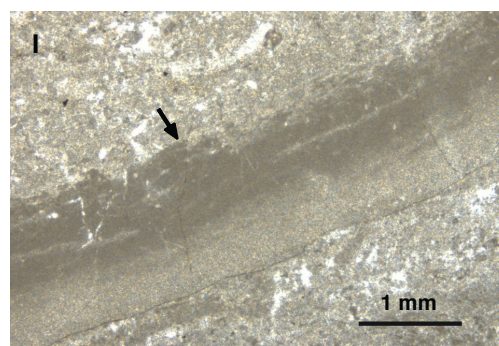
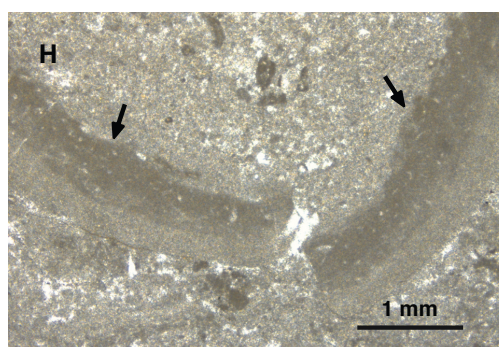


Figure 4 continued

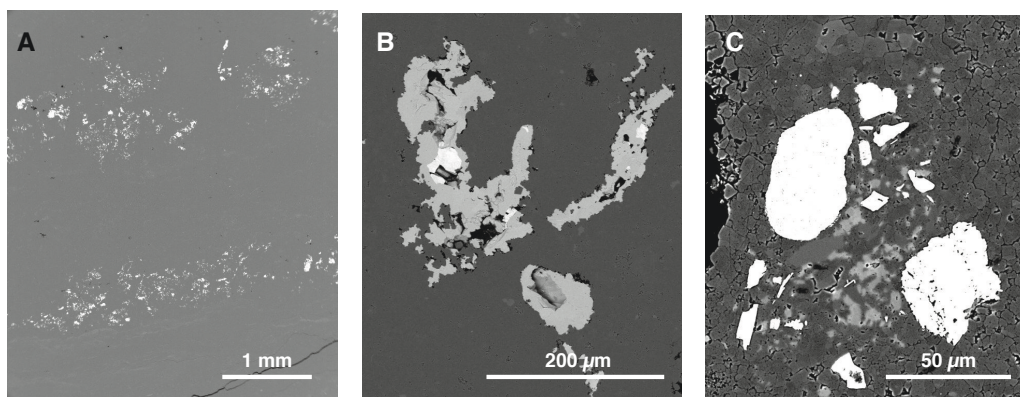


Figure 5

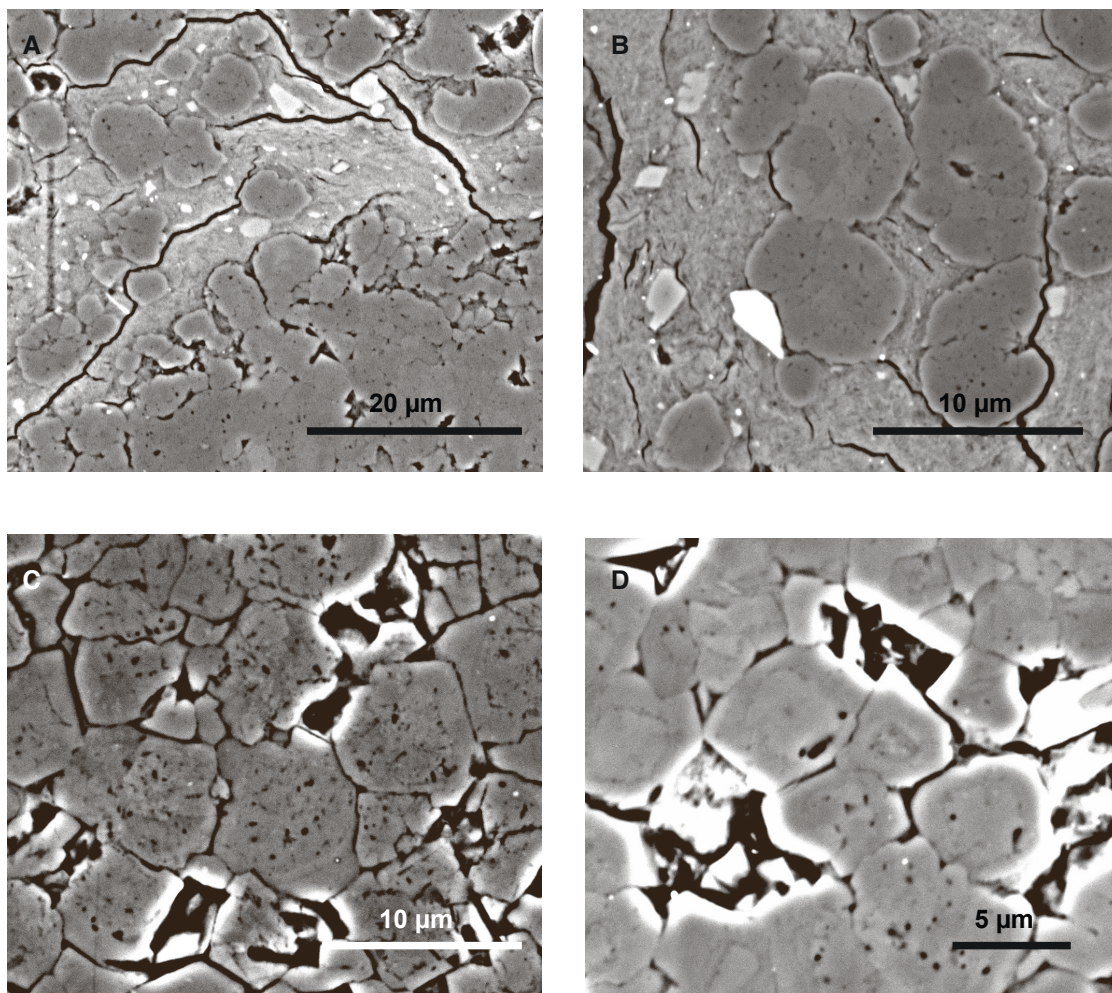


Figure 6

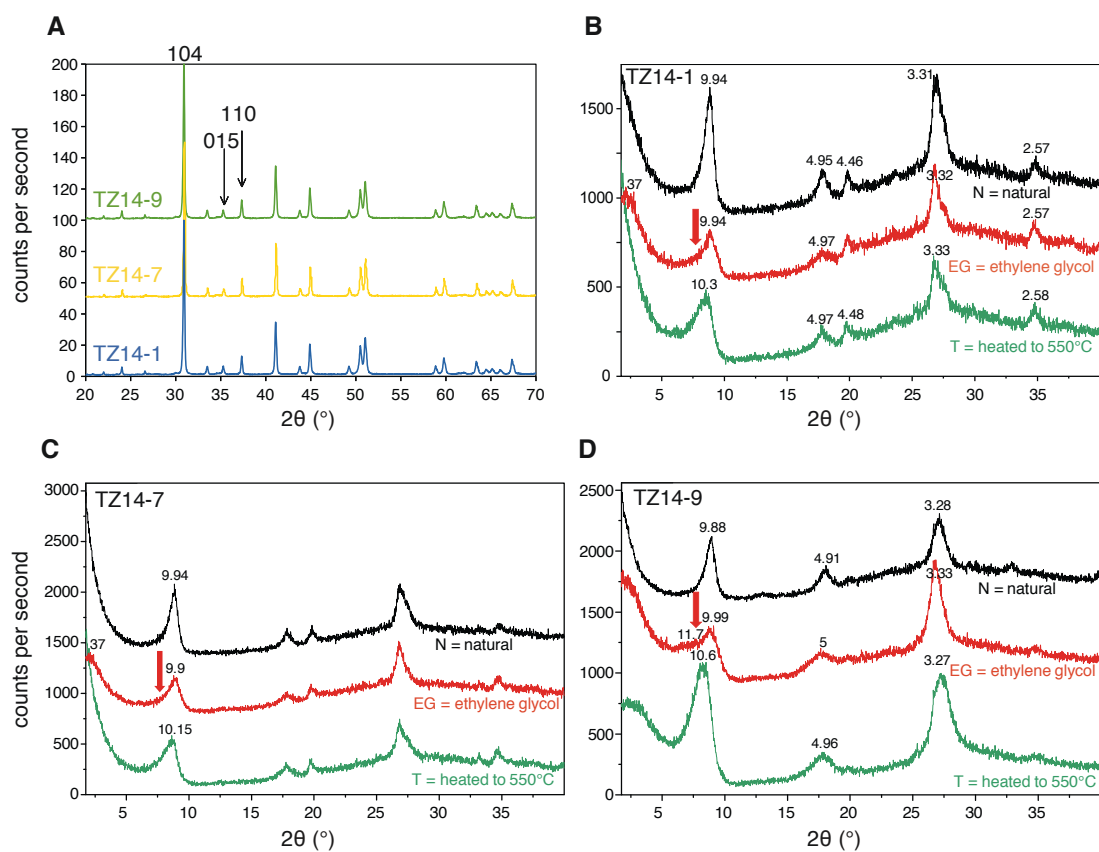


Figure 7

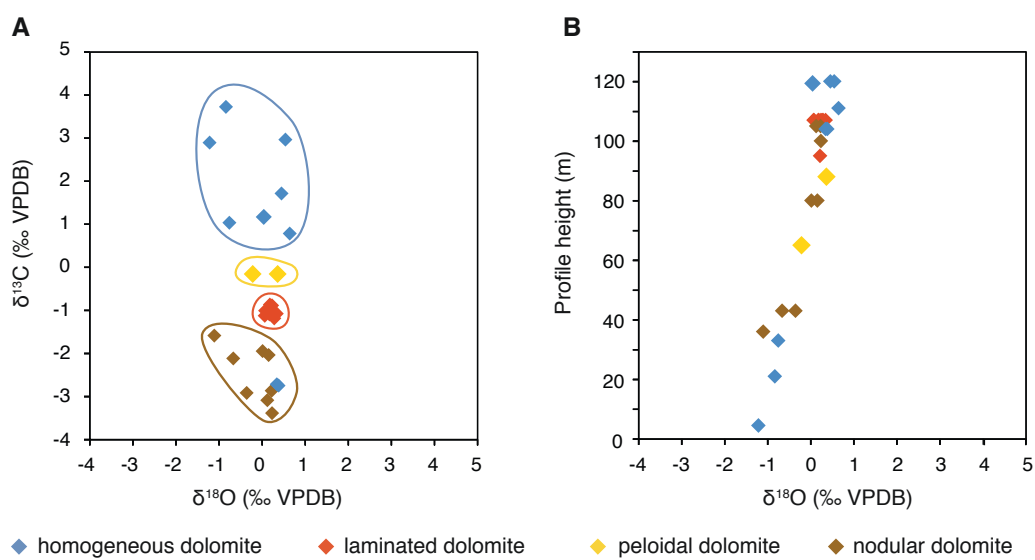


Figure 8

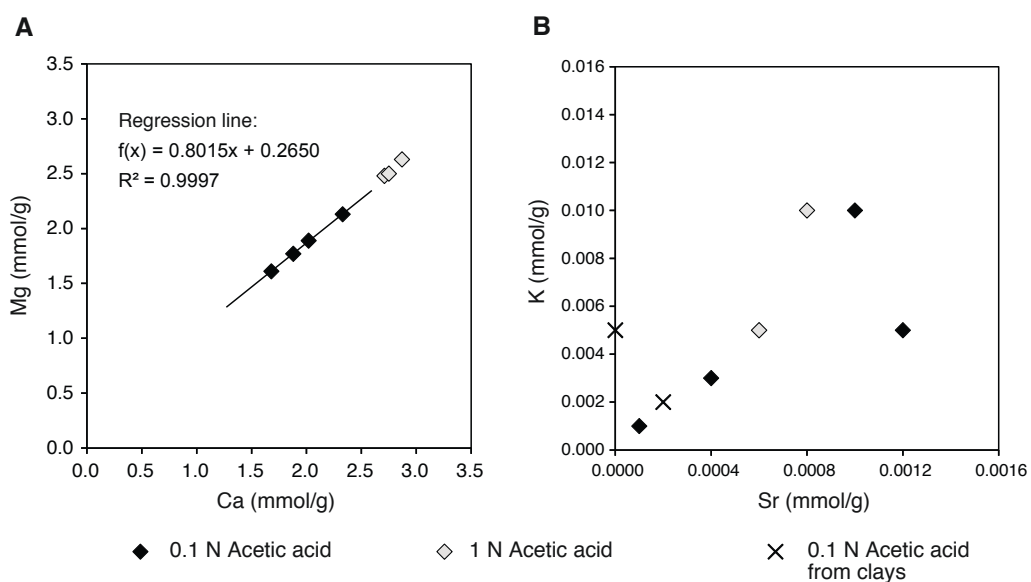


Figure 9

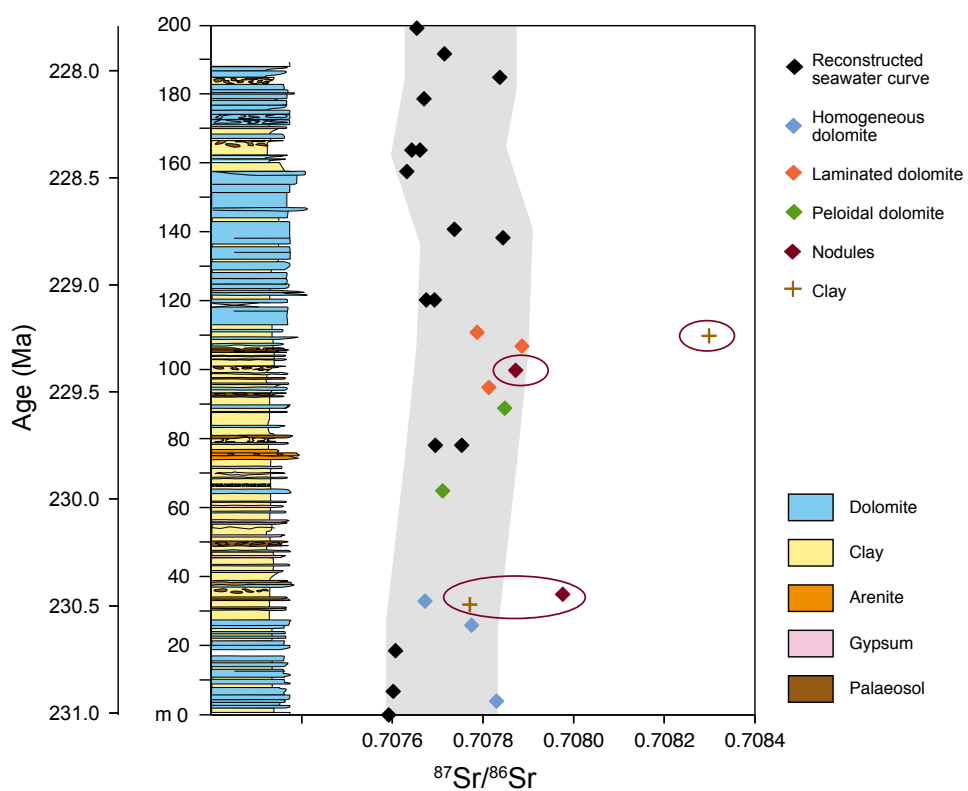


Figure 10

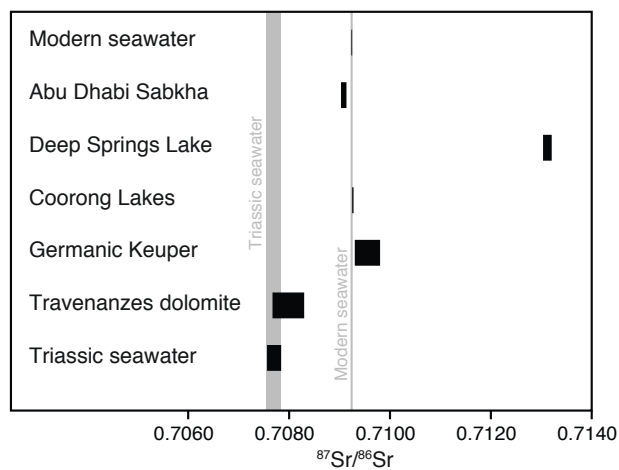


Figure 11



Table 1

Macroscopic Description	Height	Samples		Matrix			Allochthems			Sedimentary structures			Porosity			Deformation		SMF**				
		2014	2016	Aphano- topic	Micro- spar	Cavity- filling	Undeform. mud clasts	Deformed mud clasts	Fiat pebbles	Packed pebbles	Ooids	Quartz clasts	Bioclasts	Lamination	Graded Bedding	Pseudo- bedding	Erosion surfaces		Fenestral Porosity	Moldic porosity	Soil sediment deformation	Brittle deformation
dolomite with pyrite	120.0		TZ16-22	+	+	+	++	+	-	-	-	-	-	+	-	-	-	+	+	+	++	25
laminated dolomite/clay	111.0	TZ14-11	TZ16-20	++	+	+	+	+	+	-	-	-	-	+	+	+	-	+	-	+	++	25
laminated dolomite	107.0	TZ14-10	TZ16-21/S3	++	+	+	+	+	+	-	-	-	-	++	+	+	+	+	-	+	++	25
laminitic	107.0		TZ16-17	++	+	-	+	+	+	-	-	-	-	±	-	-	-	+	+	+	+	25
dolomite nodule	105.0		TZ16-S2	++	+	-	+	+	+	-	-	-	-	±	-	-	-	+	+	+	+	diag.
homogeneous dolomite	104.0		TZ16-S1	++	+	±	+	+	±	-	-	-	-	-	-	-	-	-	-	+	+	23
nodular dolomite	100.0	TZ14-13		++	+	-	++	+	±	-	-	-	-	-	-	-	-	-	-	±	+	diag.
dolomite nodule	96.0		TZ16-15	++	±	+	++	+	±	-	-	-	-	-	-	-	-	-	-	±	++	diag.
laminated dolomite	95.0	TZ14-9		+	-	+	+	+	±	-	-	-	-	+	+	+	+	+	-	+	++	25
porous dolomite	89.0	TZ14-12		+	±	-	+	+	±	-	-	-	-	+	+	+	+	+	-	+	++	23
nodular bed	80.0		TZ16-13	++	+	+	+	+	-	-	-	-	-	-	-	-	-	-	-	+	+	diag.
palaeosol, nodule	79.0		TZ16-12	++	±	±	+	+	-	-	-	-	-	-	-	-	-	-	-	++	++	diag.
sandy dolomite (congl.)	74.0	TZ14-5	TZ16-11	++	±	±	++	+	++	-	-	-	-	-	-	-	-	±	±	-	-	23
sandstone	74.0		TZ16-10	+	±	±	++	+	+	-	-	-	-	-	-	-	-	±	±	-	-	25
brittle porous dolomite	65.0	TZ14-4		+	+	+	+	-	-	+	+	-	-	-	-	-	-	+	+	+	+	15
porous dolomite	49.0		TZ16-7	++	±	+	±	-	-	-	-	-	-	-	-	-	-	±	±	+	+	23
nodules of dolomite	35.0	TZ14-3		++	±	-	±	-	-	-	-	-	-	-	-	-	-	-	-	+	+	diag.
dolomite nodule	35.0	TZ14-2		+	±	-	-	±	±	-	-	-	-	-	-	-	-	-	-	+	+	diag.
arenite	33.5		TZ16-8	+	±	-	-	-	++	-	-	-	-	-	-	-	-	-	-	+	+	Sst
homogeneous dolomite	33.0	TZ14-1		++	±	-	+	+	±	-	-	-	-	±	±	±	±	-	-	+	+	23
laminated dolomite	31.5		TZ16-2	+	-	-	+	-	-	-	-	-	-	+	+	+	+	+	-	±	±	Sst
palaeosol, dolomit	30.1		TZ16-3	++	-	-	±	-	-	-	-	-	-	-	-	-	-	-	-	+	+	diag.
red mottled dolomite	26.0	TZ14-7		-	-	-	±	-	-	-	-	-	-	-	-	-	-	-	-	±	±	23
dolomite with clay	21.0	TZ14-8		++	-	-	±	-	-	-	-	-	-	±	±	±	±	-	-	±	±	23
homogeneous dolomite	4.0	TZ14-6		++	+	±	+	-	-	-	-	-	-	+	+	+	+	-	-	+	±	25

** Nodules are most likely diagenetic and can thus not be associated to a microfacies

(+) putative

++ very abundant

+ common

± rare

- not present

* Needs to be further subdivided into pebbles, intracrysts, flat pebbles and clast of brittle deformation

□ Sandstone

□ Oolithic dolomite

□ Nodular dolomite

□ Laminated dolomite

□ Homogeneous dolomite



Table 2

Sample	Depth (m)	d(A°)	Ca/(Ca+Mg) (%)	015/110
TZ14-1	33.0	2.88944	51.1	0.44
TZ14-7	43.0	2.88871	50.9	0.41
TZ14-9	95.0	2.88633	50.1	0.46



Table 3

Sample	TC (wt%)	TOC (wt%)	TIC (wt%)
TZ16-1	0.06	0.05	0.02
TZ16-19B	0.12	0.11	0.02
TZ16-5	0.16	0.05	0.12
TZ16-19A	0.34	0.10	0.25
TZ16-14	0.42	0.16	0.27
TZ16-18	0.50	0.07	0.43
TZ16-16	0.51	0.05	0.46



Table 4

Sample	Depth (m)	$\delta^{13}\text{C}$ (‰ VPDB)	$\delta^{18}\text{O}$ (‰ VPDB)	Type	Description
TZ14-1	33	1.04	-0.76	homogeneous	with siliciclastis
TZ14-3	35	-1.58	-1.11	nodule	with barite
TZ14-4	65	-0.15	-0.22	peloidal	with apatite
TZ14-6	4	2.90	-1.22	homogeneous	with siderite and pyrite
TZ14-8	21	3.73	-0.84	homogeneous	with clay, apatite and Fe-oxide
TZ14-9	95	-1.01	0.21	laminated	with celestine and barite
TZ14-10b	107	-1.05	0.26	laminated	with apatite and pyrite
TZ14-11	111	0.79	0.64	homogeneous	homog. Lamina with clay and pyrite
TZ14-12	89	-0.15	0.36	peloidal	with megalodont and Ti-oxides
TZ14-13	100	-3.38	0.23	nodule	palaeosol with Fe-oxide
TZ16-St1	104	-2.74	0.38	homogeneous	mud clast top
	104	-2.71	0.34	homogeneous	matrix
TZ16-St2	105	-3.08	0.12	nodule	matrix top
	105	-2.86	0.22	nodule	matrix bottom
TZ16-7	43	-2.91	-0.36	<i>Rauhwacke</i>	matrix top
	43	-2.11	-0.67	<i>Rauhwacke</i>	matrix bottom
TZ16-13	80	-2.03	0.15	nodule	matrix top
	80	-1.94	0.01	nodule	matrix bottom
TZ16-21	107	-0.86	0.18	laminated	graded lamina
	107	-1.09	0.17	laminated	ligh lamina
	107	-0.88	0.23	laminated	dark lamina
TZ16-22	120	1.72	0.45	homogeneous	mud clast
	120	1.22	0.15	homogeneous	lamination
	120	2.97	0.54	homogeneous	homogeneous part
TZ16-St3	107	-1.07	0.34	laminated	dark layer, lense
	107	-1.00	0.07	laminated	dark layer bottom
	107	-1.18	0.28	laminated	dark layer top
	107	-1.12	0.06	laminated	light layer top



Table 5

Sample	Element	0.1 N acetic acid fraction				1 N acetic acid fraction			1 N HCl fraction	
		$\mu\text{mol/g}$	$\mu\text{mol/g}$	$\mu\text{mol/g}$	$\mu\text{mol/g}$	$\mu\text{mol/g}$	$\mu\text{mol/g}$	$\mu\text{mol/g}$	$\mu\text{mol/g}$	$\mu\text{mol/g}$
Bulk dolomite samples										
		TZ14-1 0.098 g	TZ14-7 0.127 g	TZ14-9 0.099 g	crystal 0.094 g	TZ14-1 0.098 g	TZ14-7 0.127 g	TZ14-9 0.099 g		
	Al	6.58	3.17	11.57	3.04	4.51	8.17	5.97		
	Ca (mmol/g)	1.68	2.33	1.88	2.50	2.87	2.71	2.75		
	Fe	4.97	3.53	10.67	34.27	2.04	9.15	5.02		
	K	3.32	9.71	5.26	0.93	10.31	4.65	13.51		
	Mg (mmol/g)	1.61	2.13	1.77	2.34	2.64	2.48	2.50		
	Mn	5.96	3.57	7.68	15.24	10.84	3.72	10.67		
	Na	12.78	18.98	17.32	1.85	17.35	20.12	23.30		
	P	1.50	n.d.	0.98	n.d.	0.20	1.45	n.d.		
	Ti	n.d.	n.d.	n.d.	n.d.	n.d.	n.d.	n.d.		
	Ba	0.50	0.03	0.48	n.d.	1.75	0.02	1.03		
	Sr	0.38	1.00	1.16	0.13	0.79	0.57	34.91		
	Rb	n.d.	n.d.	n.d.	n.d.	n.d.	n.d.	n.d.		
Clay samples										
		TZ16-1 0.038 g	TZ16-19B 0.030 g			TZ16-1 0.038 g	TZ16-19B 0.030 g		TZ16-1 0.038 g	TZ16-19B 0.030 g
	Al	2.18	4.52			1.54	4.01		39.86	33.62
	Ca	19.14	11.62			8.48	4.34		0.71	0.60
	Fe	0.72	1.79			0.83	2.25		75.59	11.56
	K	4.97	9.02			2.77	3.69		11.69	12.61
	Mg	8.05	13.76			4.46	6.07		24.62	18.75
	Mn	n.d.	n.d.			n.d.	n.d.		n.d.	n.d.
	Na	0.355	0.470			0.305	0.389		0.531	0.828
	P	6.89	1.08			0.67	n.d.		n.d.	n.d.
	Ti	n.d.	n.d.			n.d.	n.d.		1.305	0.194
	Ba	n.d.	n.d.			n.d.	n.d.		0.022	n.d.
	Sr	0.417	0.047			0.187	0.018		0.017	0.005
	Rb	n.d.	n.d.			n.d.	n.d.		n.d.	n.d.



Table 6. Sr-isotopes

Sample	Section (m)	Description	Seq. extr.	Weight (mg)	Reagent	Amount (ml)	Extr. T (°C)	Extr. time	Shaker y/n	Washing (before step)	Run no.	⁸⁷ Sr/ ⁸⁶ Sr	2σ (10 ⁻⁴)	Aliquot for conc.
NBS987		Standard solution (500 ppm)		500 ng							(n = 40)	0.710272	4	
NBS988		Standard solution (500 ppm)		500 ng							(n = 9)	0.710268	6	
Test minerals														
<i>Series 1 (sequential extraction)</i>														
Celestine				2.34	1M NaCl	2 ml	20	12 h	n	1M NaCl	6052	0.708037	5	
Barite				25.09	0.1N AcOH	2 ml	20	12 h	n	3M NaCl, 1M KCl, H ₂ O, 0.1N AcOH	6109	0.708867	9	
Dolomite				9.88	0.1N AcOH	2 ml	20	12 h	n	3M NaCl, 1M KCl, H ₂ O, 0.1N AcOH	6110	0.709942	11	
Mixture		Barite 4.5 mg; Celestine 8.91 mg; Dolomite 35.9 mg	seq.	49.31	1M NaCl	2 ml	20	12 h	n	0.1N AcOH	6053	0.708038	3	
Mixture			seq.	-	0.1N AcOH	2 ml	20	12 h	n	3M NaCl, 1M KCl, H ₂ O, 0.1N AcOH	6108	0.709501	40	
<i>Series 2</i>														
Celestine				2.22	1M NaCl	2 ml	20	2 h	n	-	6121	0.708045	4	
Celestine				4.60	0.1N AcOH	2 ml	20	4 h	n	12h 1M NaCl	6132	0.708047	3	
Barite			seq.	36.94	6N HCl	2 ml	40	12 h	n	-	6152	0.707610	5	
Barite			seq.	-	6N HCl	2 ml	40	12 h	n	-	6155	0.707564	6	
Dolomite				17.37	0.1N AcOH	5 ml	40	12 h	n	-	6068	0.710831	7	
Dolomite		Replicate		3.41	0.1N AcOH	2 ml	40	12 h	n	-	6114	0.710557	11	
Tavananzes Fm.														
<i>Bulk samples sequential extractions, Series 1</i>														
TZ14-1	33 m	homogeneous dolomite	seq.	12.35	1M NaCl	2 ml	20	12 h	n	-	6112	0.708125	12	
TZ14-1	33 m	homogeneous dolomite	seq.	-	0.1N AcOH	3 x 2 ml	20	4h, 12h, 4h	y	1M NaCl, H ₂ O, 3.3M KCl, H ₂ O	6169	0.707666	4	
TZ14-1	33 m	homogeneous dolomite	seq.	-	0.1N AcOH	2 ml	20	36 h	y	-	6173	0.715417	250	
TZ14-9	95 m	laminated dolomite	seq.	13.50	1M NaCl	2 ml	20	12 h	n	-	6113	0.707880	4	
TZ14-9	95 m	laminated dolomite	seq.	-	0.1N AcOH	3 x 2 ml	20	4h, 12h, 4h	y	1M NaCl, H ₂ O, 3.3M KCl, H ₂ O	6171	0.707817	5	
TZ14-9	95 m	laminated dolomite	seq.	-	0.1N AcOH	2 ml	20	36 h	y	-	6174	0.719226	455	
Mixture		Residue from test mineral series 1	seq.	-	0.1N AcOH	3 x 2 ml	20	4h, 12h, 4h	y	1M NaCl, H ₂ O, 3.3M KCl, H ₂ O	6172	0.709812	5	
Mixture		Residue from test mineral series 1	seq.	-	0.1N AcOH	2 ml	20	36 h	y	-	6176	0.709900	4	
TZ14-1	33 m	homogeneous dolomite		42.76	0.1N AcOH	2 ml	20	4 h	n	-	6130	0.707894	4	
TZ14-9	95 m	laminated dolomite		17.69	0.1N AcOH	2 ml	20	4 h	n	-	6131	0.707872	5	
<i>Bulk samples sequential extractions, Series 2</i>														
TZ14-1	33 m	homogeneous dolomite		93.91	1M NaCl	10 ml	20	12 h	y	-	6182	0.708096	5	
TZ14-1	33 m	homogeneous dolomite	seq.	98.28	0.1N AcOH	10 ml	20	12 h	y	-	6183	0.707812	4	yes
TZ14-1	33 m	homogeneous dolomite	seq.	-	1N AcOH	10 ml	20	12 h	y	-	6205	0.707670	5	yes
TZ14-1	33 m	homogeneous dolomite		50.00	6N HCl	5 ml	20	12 h	n	10h 1N CH ₃ COOH	6445	0.710403	6	
TZ14-7	26 m	mottled dolomite		90.64	1M NaCl	10 ml	20	12 h	y	-	6179	0.707883	4	
TZ14-7	26 m	mottled dolomite	seq.	127.52	0.1N AcOH	10 ml	20	12 h	y	-	6178	0.707801	4	yes
TZ14-7	26 m	mottled dolomite	seq.	-	1N AcOH	10 ml	20	12 h	y	-	6207	0.707719	4	yes
TZ14-7	26 m	mottled dolomite		50.00	6N HCl	5 ml	20	12 h	n	10h 1N CH ₃ COOH	6449	0.730453	5	
TZ14-9	95 m	laminated dolomite		97.82	1M NaCl	10 ml	20	12 h	y	-	6187	0.707869	3	yes
TZ14-9	95 m	laminated dolomite	seq.	98.76	0.1N AcOH	10 ml	20	12 h	y	-	6185	0.707862	3	yes
TZ14-9	95 m	laminated dolomite	seq.	-	1N AcOH	10 ml	20	12 h	y	-	6206	0.707813	3	yes
TZ14-9	95 m	laminated dolomite		50.00	6N HCl	5 ml	20	12 h	n	10h 1N CH ₃ COOH	6447	0.708464	4	
Dolomite (single crystal)		control		116.65	1M NaCl	10 ml	20	12 h	y	-	6184	0.708401	40	
Dolomite (single crystal)		control	seq.	94.12	0.1N AcOH	10 ml	20	12 h	y	-	6180	0.707735	6	yes
Dolomite (single crystal)		control	seq.	-	1N AcOH	10 ml	20	12 h	y	-	6208	0.707666	6	yes
<i>Micro-drill samples</i>														
TZ14-3	35 m	dolomite nodule		-	0.1N AcOH	2 ml	20	24 h	n	H ₂ O, 5min 0.1N AcOH	6548	0.707976	4	
TZ14-4	65 m	peloidal dolomite		-	0.1N AcOH	2 ml	20	24 h	n	H ₂ O, 5min 0.1N AcOH	6549	0.707711	4	
TZ14-6	4 m	homogeneous dolomite		-	0.1N AcOH	2 ml	20	24 h	n	H ₂ O, 5min 0.1N AcOH	6550	0.707830	4	
TZ14-8	21 m	dolomite with clay		-	0.1N AcOH	2 ml	20	24 h	n	H ₂ O, 5min 0.1N AcOH	6551	0.707821	4	
TZ14-10b	107 m	laminated dolomite		-	0.1N AcOH	2 ml	20	24 h	n	H ₂ O, 5min 0.1N AcOH	6554	0.707886	4	
TZ14-11	111 m	laminated dolomite		-	0.1N AcOH	2 ml	20	24 h	n	H ₂ O, 5min 0.1N AcOH	6553	0.707787	4	
TZ14-12	89 m	peloidal dolomite		-	0.1N AcOH	2 ml	20	24 h	n	H ₂ O, 5min 0.1N AcOH	6555	0.707848	4	
TZ14-13	100 m	dolomite with palaeosol		-	0.1N AcOH	2 ml	20	24 h	n	H ₂ O, 5min 0.1N AcOH	6556	0.707872	4	
<i>Micro-drilled sequential extractions</i>														
TZ14-1	33 m	homogeneous dolomite	seq.	-	0.1N AcOH	2 ml	20	24 h	n	H ₂ O, 5min 0.1N AcOH	6411	0.707672	3	
TZ14-1	33 m	homogeneous dolomite	seq.	-	1N AcOH	20	24 h	24 h	n	H ₂ O, 5min 0.1N AcOH	6448	0.708300	23	
TZ14-7	26 m	mottled dolomite	seq.	-	0.1N AcOH	2 ml	20	24 h	n	H ₂ O, 5min 0.1N AcOH	6479	0.707775	6	
TZ14-7	26 m	mottled dolomite	seq.	-	1N AcOH	20	24 h	24 h	n	H ₂ O, 5min 0.1N AcOH	6444	0.708502	22	
TZ14-7	26 m	clay layer	seq.	-	0.1N AcOH	20	24 h	24 h	n	H ₂ O, 5min 0.1N AcOH	6410	0.707742	4	
TZ14-7	26 m	clay layer	seq.	-	1N AcOH	20	24 h	24 h	n	H ₂ O, 5min 0.1N AcOH	6446	0.708467	2	
TZ14-9	95 m	laminated dolomite	seq.	-	0.1N AcOH	2 ml	20	24 h	n	H ₂ O, 5min 0.1N AcOH	6412	0.707813	149	
TZ14-9	95 m	laminated dolomite	seq.	-	1N AcOH	20	24 h	24 h	n	H ₂ O, 5min 0.1N AcOH	6443	0.708281	56	
<i>Clay samples</i>														
TZ16-1	32 m	red (green) clay	seq.	38.30	0.1N AcOH	2 ml	20	12 h	n	2h 0.1N AcOH	6557	0.707771	4	yes
TZ16-1	32 m	red (green) clay	seq.	-	1N AcOH	2 ml	20	12 h	n	2h 1N AcOH	6558	0.707768	4	yes
TZ16-1	32 m	red (green) clay	seq.	-	6N HCl	2 ml	20	12 h	n	4h 6N HCl	6559	0.722998	18	yes
TZ16-19B	110 m	dark grey clay	seq.	29.74	0.1N AcOH	2 ml	20	12 h	n	2h 0.1N AcOH	6560	0.708299	8	yes
TZ16-19B	110 m	dark grey clay	seq.	-	1N AcOH	2 ml	20	12 h	n	2h 1N AcOH	6561	0.708582	8	yes
TZ16-19B	110 m	dark grey clay	seq.	-	6N HCl	2 ml	20	12 h	n	4h 6N HCl	6552	0.733910	24	yes
<i>Germanic Keuper</i>														
Lehr		micro-drilled		-	0.1N AcOH	2 ml	20	24 h	n	H ₂ O, 5min 0.1N AcOH	6545	0.708303	4	
Kou 1-2 B		micro-drilled		-	0.1N AcOH	2 ml	20	24 h	n	H ₂ O, 5min 0.1N AcOH	6546	0.708805	6	
<i>Deep Springs Lake</i>														
DS11-3, 16.5	16.5 cm	dried mud	seq.	91.17	0.1N AcOH	10 ml	20	5 min	n	H ₂ O	6363	0.713207	4	
DS11-3, 16.5	16.5 cm	dried mud	seq.	-	0.1N AcOH	10 ml	20	10 h	n	H ₂ O	6363	0.713086	4	
DS11-3, 52.5	52.5 cm	dried mud	seq.	62.19	0.1N AcOH	10 ml	20	10 h	n	H ₂ O	6343	0.713035	4	
<i>Milne Lake (Coorong)</i>														
CM01-3	30 cm	dried mud, ground	seq.	47.94	0.1N AcOH	10 ml	20	5 min	n	H ₂ O	6340	0.709251	4	
CM01-3	30 cm	dried mud, ground	seq.	-	0.1N AcOH	10 ml	20	10 h	n	H ₂ O	6340	0.709275	3	
CM01-9	90 cm	dried mud, ground	seq.	52.47	0.1N AcOH	10 ml	20	10 h	n	H ₂ O	6341	0.709272	4	